Journal of Materials Research and Technology 43 (2026) 6198–6223

Contents lists available at ScienceDirect

Journal of Materials Research and Technology

journal homepage: www.elsevier.com/locate/jmrt

A sequential functional coating on magnesium alloy: Plasma electrolytic oxidation layer for sustained osteogenic icariin and rapid antibacterial peptide delivery

Binbin Wang [a], Hao Zhang [a,*], Xiaolong Shen [b], Jiaping Han [a,**], Jiaxin Chen [a], Rifang Luo [c], Yunbing Wang [c], Da Qing Li [d,***], Yingqi Chen [e,****]

[a] Vanadium and Titanium Critical Strategic Materials Key Laboratory of Sichuan Province, Panzhihua University, Panzhihua, 617000, China
[b] College of Biology & Chemical Engineering (Agricultural College), Panzhihua University, Panzhihua, 617000, China
[c] National Engineering Research Center for Biomaterials, Sichuan University, Chengdu, 610064, Sichuan, China
[d] Lifeline Medical Group Li Daqing Vascular Access Center, Xi'an, 710000, Shaanxi, China
[e] Medical Innovation Technology Transformation Center of Shenzhen Second People's Hospital, the First Affiliated Hospital, Shenzhen University, Shenzhen, 518055, China

ARTICLE INFO

Keywords:
Mg alloys
Sequentiality
Plasma electrolytic oxidation
AMPs
ICA

ABSTRACT

An icariin/polytrimethylene carbonate (ICA/PTMC) composite coating was constructed on the surface of plasma electrolytic oxidized (PEO) AZ31 alloy, followed by chemical grafting of antimicrobial peptides (AMPs). The PEO coating served as a corrosion-resistant framework, while ICA—a flavonoid compound extracted from the traditional Chinese herb *Epimedium*—was physically encapsulated with PTMC. ICA can promote bone healing via the Wnt/β-catenin pathway. The outermost layer was functionalized with chemically grafted AMPs to mitigate infection risks following magnesium alloy bone implantation. Results demonstrated that nitrogen (N) element was detected in the coating by EDS and XPS, and FT-IR spectroscopy revealed the characteristic C═O stretching peak of flavonoids, confirming the successful loading of AMPs and ICA. Compared with bare AZ31 ($i_{corr} = 2.57 \times 10^{-5}$ A/cm^2) and PEO coating (1.61×10^{-6} A/cm^2), the PEO-P@I-A coating exhibited a much lower corrosion current of 1.54×10^{-9} A/cm^2 and an impedance modulus exceeding 10^7 Ω cm^2 at 10^{-2} Hz. During 21 days of immersion in SBF, the system effectively retarded the degradation rate, with a hydrogen evolution rate of 0.036 mL cm^{-2}·day^{-1}. In vivo implantation experiments showed stable degradation of the implant within 8 weeks, as evidenced by X-ray and Micro-CT imaging that revealed no gas-induced cavities or osteolysis, with active new bone formation and good osseointegration; no signs of infection were observed. The incorporation of AMPs endowed the coating with superior antibacterial activity during the early implantation stage. This anti-infection function, together with the sustained release of ICA from the underlying layer, synergistically created a favorable microenvironment that supported osteogenic, angiogenic, and anti-inflammatory effects, ultimately promoting bone regeneration. This study provides a novel strategy for the surface modification of degradable magnesium-based bone implants, holding promising application prospects.

1. Introduction

Mg and its alloys are widely considered to be potentially revolutionary materials for orthopaedic implants, owing to their biodegradability, biocompatibility, and ideal Young's modulus (approximately 45 GPa), which closely matches that of natural cortical bone [1–5]. Significantly, a growing body of evidence has been suggesting that Mg ions released by Mg-based bone implants can stimulate bone regeneration and hasten healing [6–8]. The primary barrier to the clinical application of Mg and its alloys is their high reactivity within

* Corresponding author.
** Corresponding author.
*** Corresponding author.
**** Corresponding author.
E-mail addresses: zhanghaozi25@163.com (H. Zhang), hanjiaping88@126.com (J. Han), 1270448171@qq.com (D.Q. Li), yqchen0203@foxmail.com (Y. Chen).

https://doi.org/10.1016/j.jmrt.2026.07.118
Received 27 May 2026; Received in revised form 6 July 2026; Accepted 14 July 2026
Available online 15 July 2026
2238-7854/© 2026 The Authors. Published by Elsevier B.V. This is an open access article under the CC BY-NC-ND license (http://creativecommons.org/licenses/by-nc-nd/4.0/).

physiological environment [9,10]. Rapid degradation results in swift loss of mechanical integrity, production of excessive hydrogen, creation of a local alkaline environment, and accumulation of corrosion products, all of which can negatively affect bone-tissue repair to varying degrees [11]. An ideal absorbable bone implant must strike an optimal balance between mechanical stability, fracture healing, and degradation [12,13]. From the standpoint of the interplay between mechanical stability and degradation, the implant's degradation rate should be low during the initial three to six months, while its mechanical stability should be high to support bone healing [14]. During fracture healing, inflammation and hematoma formation start within 1-7 days, leading to the development of granulation tissue. Within 2 to 4 weeks, cartilage emerges from the granulation tissue and subsequently transforms into a hard callus over the following 2 to 4 months, establishing a stable structure around the fracture site. Over several months to years, the mineralized callus gradually regenerates, ultimately forming a structure that closely resembles the original bone morphology [15–17].

Consequently, Mg-based bone implants should exhibit an appropriate degradation rate to align with the support needed for bone-tissue healing (the specific duration varies depending on the implant site and condition of adjacent soft tissues, among other factors) [18,19]. Concurrently, they should sequentially exhibit multiple functions such as early antibacterial effects and mid-to-late osteoinduction, and meet the clinical application requirements of the bone-repair process [20,21]. Currently, achieving such temporally coordinated functions for Mg-based bone implants remains at an early stage of development [22,23]. From the perspective of complete temporal and spatial interactions between Mg-based bone implants and the human environment, and in response to clinical application requirements, constructing multi-level composite coatings is the main development trend for the future [24]. This involves, on the basis of slowing down the rapid degradation of the base material, achieving spontaneous sequential functional switching of early antibacterial effects and subsequent osteoinduction [25].

Constructing a multi-functional composite coating on Mg surface is an effective strategy to achieve this goal. Top-down sequential degradation coating is a surface-modification method that has emerged in the recent years. Its design concept is to build a multi-level structure on the Mg surface to achieve multi-functionality: selecting pre-treatment methods to enhance the corrosion resistance of the system and modify the surface, promoting the subsequent coating deposition; and constructing a gradient coating with special biological functionality on the surface of the pretreatment layer [26]. The plasma electrolytic oxidation (PEO) process is a relatively simple technique that utilizes aqueous electrolytes and generates significantly less hazardous waste compared to conventional anodizing or chemical conversion coatings, making it an environmentally friendly pretreatment method. [27–29]. This technology uses high voltage to create controllable in-situ grown ceramic layers on the surface of Mg alloys, which exhibit strong substrate bonding and good corrosion resistance [30]. Simultaneously, the addition of appropriate elements (such as calcium, phosphorus, and strontium) to the electrolyte effectively promotes the proliferation and differentiation of bone-related cells. However, the high porosity of the PEO coating provides a penetration channel for corrosion ions, which is not conducive to the long-term protection. Modifying the PEO surface with multiple components and facilitating interactions among the components to enhance the performance of the system are key challenges faced by the sequential-degradation coatings [31,32].

Polytrimethylene carbonate (PTMC) is a biodegradable medical material with good biocompatibility and surface-erosion characteristics. In particular, its surface-erosion mode is more conducive to the long-term corrosion control of Mg alloys [33,34]. PTMC can be used as a drug carrier for local administration. Icariin (ICA) is a typical flavonoid compound isolated from epimedium, which has multiple biological effects such as anti-inflammatory, antibacterial, and anti-cancer effects and promotes bone formation, which can regulate bone homeostasis. Bone homeostasis primarily reflects three balances based on osteogenic/adipogenic differentiation of bone marrow mesenchymal stem cells (BMSCs): skeletal-immune balance, oxidation-antioxidation balance, and iron metabolism balance. ICA, as one of the common components of traditional Chinese medicine, exhibits fewer adverse reactions and has been studied for its application in scaffold implantation [35–42]. In addition, ICA can promote angiogenesis and migration of BMSCs through multiple signalling pathways (Wnt/β-catenin) in bone-marrow mesenchymal stem cells, thereby promoting the proliferation and osteogenesis of bone cells [43–47]. Furthermore, to realize antibacterial function during the initial period, antimicrobial peptides (AMPs) are grafted onto the surface. AMPs are a new type of antibacterial agent, with efficient and broad-spectrum antibacterial properties, which can be metabolized in the human body, and are not prone to developing antibiotic resistance. In recent years, AMPs have been frequently used as key components for the surface modification of implants to enhance their antibacterial performance [48–51]. Although AMPs may be degraded by enzymes in the body, covalent fixation on the implant surface can stabilize their antibacterial effect in the body and weaken the degradation effect of enzymes. AMPs have been proven to be able to bond with hydroxyl and other groups to form relatively stable structures, which improves their feasibility for chemical deposition and co-deposition with other organic components [52–55].

To meet the multi-functional requirements of Mg-based bone implants, a composite coating is constructed on the surface of AZ31 alloy. The coating system is composed of a PEO layer, a PTMC coating loaded with ICA, and AMPs. First, the PEO layer is used to slow down the corrosion rate of the AZ31 substrate, and a PTMC coating loaded with ICA is deposited on the surface of the PEO layer. The proliferation of osteoblasts is induced by ICA to promote bone healing. To further endow it with the antibacterial function in the initial stage of implantation, AMPs are chemically grafted on the surface, thereby achieving the construction of a sequential multi-functional coating on the surface of degradable Mg-based bone implants. The construction of the coating system and performance, including corrosion behaviour and in-vitro and in-vivo bio-properties are systematically investigated, and the sequential degradation and superiority of the multi-functional coating are discussed in detail.

2. Materials and methods

2.1. Material preparation methods

The AZ31 alloy rods (supplied by Huatai Metal Materials Co., Ltd., China) were used as substrate material, with the following chemical composition (wt.%): Al 3.0%, Zn 0.8%, and balance Mg. The rods were wire-cut into two types of disk-shaped specimens: φ10 mm × 1.5 mm and φ2.5 mm × 2.5 mm. All chemical reagents were used as received without further purification. Dopamine hydrochloride (≥98% purity, 189.64 g/mol), epigallocatechin gallate (EGCG, ≥95% purity, 458.37 g/mol), and Tris-base (≥99.9% purity, 121.14 g/mol) were purchased from Sigma-Aldrich (Shanghai, China). Absolute ethanol (analytical grade), trisodium phosphate dodecahydrate ($Na_3PO_4{\cdot}12H_2O$, analytical grade), and potassium hydroxide (KOH, analytical grade) were obtained from Chengdu Kelong Chemical Co., Ltd. Icariin (ICA, ≥95% purity) was purchased from Shanghai Macklin Biochemical Technology Co., Ltd. The antimicrobial peptide (AMPs, sequence: WRWRWR-NH_2, ≥95% purity) was provided by Hangzhou Sino Peptide Co., Ltd. For clarity, the samples are designated as follows: PEO for the PEO-treated substrate; PEO-P@I for the PEO coating further deposited with PTMC encapsulating ICA (where P=PTMC, I=ICA, and @ denotes encapsulation); and PEO-P@I-A for the final coating after grafting of AMPs (A = antimicrobial peptides).

The AZ31 samples (φ10 mm × 1.5 mm) were mechanically polished using sequential SiC sandpapers (#800-#5000 grit) prior to plasma electrolytic oxidation (PEO) treatment. PEO treatment was performed in an aqueous electrolyte containing 0.03 M $Na_3PO_4{\cdot}12H_2O$ and 0.04 M

KOH. The required mass of $Na_3PO_4{\cdot}12H_2O$ (molecular weight: 380.12 g/mol) was calculated based on its anhydrous equivalent (molecular weight: 163.94 g/mol) to achieve the target phosphate concentration, ensuring accurate molarity. The electrolyte was prepared by dissolving the calculated amounts of $Na_3PO_4{\cdot}12H_2O$ and KOH in deionized water under continuous stirring until complete dissolution. PEO electrolyte using a pulsed DC power supply (AIYS750-15A) under constant-current conditions (10 A/dm^2, 500 Hz, 300 μs pulse width, 30% duty cycle) for 6 min. During this period, the voltage progressively increased from the initial breakdown threshold to a final voltage of approximately 450-480 V, which is consistent with typical PEO parameters for magnesium alloys. The electrolyte temperature was maintained at 15-25°C. The resulting PEO-coated samples (PEO) were ultrasonically cleaned (40% power, 5 s) and dried at 40°C.

For ICA incorporation, a PTMC-assisted co-deposition method was employed. A homogeneous DMF solution containing 1.5 mg/mL ICA and 8.9 mg/mL PTMC was cast onto PEO-treated samples in Polytetrafluoroethylene molds, followed by solvent evaporation at 60°C for 12 h to obtain PEO-P@I composite coatings.

Surface functionalization for AMPs grafting involved sequential treatments: (1) 2 h immersion in 2 mg/mL DA solution at room temperature, (2) 2 h treatment with 1 mg/mL DA and 0.2 mg/mL EGCG mixture, and (3) 24 h static grafting in 2 mg/mL AMP solution at 4°C, yielding the final PEO-P@I-A composite coating. Control samples were prepared following identical protocols.

2.2. Material characterization

The prepared specimens were systematically characterized to analyse their microstructure and surface properties. For cross-sectional analysis, samples were thermally mounted to expose only the transverse section. Surface and cross-sectional morphologies were examined using field emission scanning electron microscopy (FE-SEM, Quanta FEG250, FEI, USA) coupled with energy-dispersive X-ray spectroscopy (EDS, EDAX Element, USA) for elemental composition analysis. Phase composition was determined by X-ray diffraction (XRD, D8 Advance, Bruker, Germany) with Cu Kα radiation ($\lambda = 1.5406$ Å) over a 2θ range of 10-90°. Surface functional groups were identified by Fourier transform infrared spectroscopy (FTIR, Nicolet Nexus410, Thermo Scientific, USA) in the wavenumber range of 400-4000 cm^{-1}. Chemical states of surface elements were analyzed using X-ray photoelectron spectroscopy (XPS, Smart Lab 9K, Rigaku, Japan) with Al Kα excitation (1486.6 eV) at 300 W operating power, where high-resolution spectra were deconvoluted through peak fitting. Surface wettability was evaluated via contact angle measurements (WCA2000A, Aifesi Precision Instruments, China) using 3 μL deionized water droplets, with five measurements taken at different locations and averaged for each sample. All characterizations were performed at ambient temperature.

2.3. Corrosion resistance evaluation

Electrochemical tests and immersion experiments were conducted using simulated body fluid (SBF, pH 7.4, composition detailed in Table 1) as the electrolyte. The electrochemical characterization included potentiodynamic polarization measurements and electrochemical impedance spectroscopy (EIS) analysis. The potentiodynamic polarization scans were performed at 1 mV/s in the potential range of −2.0 V to 0 V (vs. SCE); EIS measurements were conducted at the open-circuit potential with a frequency range of 100 kHz to 10 mHz and an AC amplitude of 10 mV. The immersion tests comprised 3 parts: (1) Hydrogen evolution testing, where the SBF volume-to-sample surface area ratio was maintained at 80 mL:1 cm^2, with periodic measurement of evolved hydrogen volume normalized to the specimen surface area; (2) pH monitoring experiments conducted at a solution volume-to-surface area ratio of 50 mL:1 cm^2, with regular recording of pH variations; (3) Soak AZ31, PEO, and PEO-P@I-A samples in 45 mL of PBS buffer for 21 days. The exposed area of each sample is 0.785 cm^2. The solution is replaced every three days, and 5 mL is taken each time to evaluate magnesium ion release. All experiments were performed under controlled conditions at 37 ± 1°C with continuous agitation at 15 rpm to maintain physiological relevance.

Table 1
Simulates the composition of bodily fluids(SBF).

Ingredients	Concentration (mM)	Ions
NaCl	142.0	Na^+, Cl^-
$NaHCO_3$	4.2	HCO_3^-
KCl	5.0	K^+, Cl^-
$K_2HPO_4{\cdot}3H_2O$	1.0	HPO_4^{2-}
$MgCl_2{\cdot}6H_2O$	1.5	Mg^{2+}
$CaCl_2$	2.5	Ca^{2+}
Na_2SO_4	0.5	SO_4^{2-}
Tris + HCl	50.0	

2.4. Icariin released in vitro

PEO-P@I-A samples were soaked in phosphate-buffered saline (PBS) solution for 14 days at a constant temperature of 37°C. At 1, 3, 5, 7, and 14 days, respectively, the soaked liquid was removed, and the absorbance of the UV-VIS spectrophotometer (Jasco V-530 UV/Vis, Jasco Company, Tokyo, Japan) was measured at a wavelength of 270 nm, and the cumulative release of ICA was calculated using the ICA standard release curve according to Lambert Beer's law.

2.5. In vitro cytocompatibility evaluation

2.5.1. Cytotoxicity

Cell proliferation activity was detected by CCK-8 kit (Cell Counting Kit-8, Biyuntian Biotechnology Co., Ltd., Shanghai, China). BMSCs, HUVECs, and RAW246.7 cells were separately seeded in 24-well plates at 5 × 10^3, incubated overnight, 1 mL of extract was added, and after 3 and 5 days of continued culture, the medium was removed and 200 μL of medium and 20 μL of CCK-8 were added per well. After further incubation for 1 h, transfer 200 μL of liquid from the wells to a new 96-well plate, and measure the absorbance of each well at 450 nm using a microplate reader. Fluorescent staining was performed using live/dead cell staining kit (Calcein-AM/PI kit, Biyuntian Biotechnology Co., Ltd., Shanghai, China).

BMSCs, HUVECs, and RAW246.7 cells is seeded in 24-well plates at 5 × 10^3 and cultured overnight. 1 mL of α-MEM and DMEM was then added using 25% material extract. After continuing the culture for 3 and 5 days, add 200 μL of live/dead cell staining solution to each well plate according to the instructions. After 30 min of incubation at room temperature, the solution is removed and fluorescence images of the cells on the plate are taken with an inverted fluorescence microscope.

2.5.2. Osteogenesis and mineralization evaluation

The osteogenic effects of samples were evaluated through ALP activity assessment. BMSC cells (5 × 10^4 cells/well) were cultured in α-MEM with 10% FBS for 24h, then treated with osteogenic medium containing 25% material extract (10 mM β-glycerophosphate, 50 μg/mL ascorbic acid, 100 nM dexamethasone) for 7 days. ALP staining (Beyotime Biotechnology) visualized mineralized nodules. For mineralization analysis, cells were cultured for 21 days (medium changed every 3 days) followed by ARS staining (2% solution, pH 4.2, 37°C, 30min) to assess calcium nodule formation. All experiments were performed in triplicate with three independent repeats. Osteogenesis-related gene expression was analyzed by qPCR comparing control and extract-treated groups (7 days). RNA was extracted (TRIzol), reverse transcribed, and analyzed for ALP, Col-I, OCN, and Runx2 expression (GAPDH reference), Table S1.

2.5.3. Ferroptosis evaluation

Recent studies have shown that ferroptosis [56–59],an iron-dependent programmed cell death caused by the accumulation of lipid peroxides [60],is activated in the pathological microenvironment described above and has become one of the key mechanisms leading to a decrease in osteoblast number, impaired function, and even apoptosis [61].Intracellular glutathione depletion, inhibition of GPX4 activity, and lipid peroxide accumulation combined to exacerbate osteogenic dysfunction, ultimately hindering bone regeneration. Therefore, intervention ferroptosis pathway has become a new strategy to promote bone defect repair. Ferroptosis was assessed by Prussian Blue staining for Fe^{3+} deposition. Samples fixed with 4% paraformaldehyde were stained with 2% potassium ferrocyanide/2% HCl (1:1) for 30min, forming blue $Fe_4[Fe(CN)_6]_3$ precipitates, then counterstained with nuclear fast red (3-5min). Three groups were tested: positive control (iron-treated), negative control (iron chelator-pretreated), and test group (iron and extract treated). For cellular analysis, BMSC cells (5×10^3/well) were cultured for 24h, treated with FAC (24h), washed, then incubated with deferoxamine/extract (24h) before staining. qPCR analysis of ferroptosis genes (GPX4, SLC7A11, ACSL4, TFR1) compared three groups: control, FAC-treated (100 μM, 7d), and ICA-treated (FAC 24h pretreatment + extract 7d). RNA was extracted (TRIzol), reverse transcribed, and analyzed (SYBR Green) using GAPDH as reference, Table S2.

2.5.4. Macrophage biocompatibility

RAW 264.7 macrophages (5×10^3 cells/well) were cultured for 24h, then treated with 25% extract for 7 days. Cells were washed with PBS and lysed with TRIzol for RNA extraction. Three groups were analyzed: control, ICA-treated, and AMPs + ICA combination. After 7-day treatment, RNA was reverse transcribed (Prime Script™ RT kit) and inflammatory markers (TNF-α, IL-6, IL-10) were quantified by qPCR (SYBR Green), normalized to GAPDH, Table S3.

2.6. In vitro antibacterial experiments

2.6.1. Antibacterial evaluation

The antibacterial properties were evaluated against staphylococcus aureus (*S. aureus*) and *Escherichia coli* (*E. coli*, strain CMCC(B)26003; Huan kai Microbial Sci. & Tech., Guangzhou, China). Bacterial cultures were grown overnight at 37°C with shaking (120 rpm) in tryptic soy broth (TSB; Huan kai Microbial Sci. & Tech.) to reach logarithmic phase. The bacterial suspensions were then adjusted to a density of 6×10^4 CFU/mL in fresh medium. Prior to testing, all samples were sterilized under UV irradiation. Subsequently, 50 μL of bacterial suspension was inoculated onto each material surface and incubated at 37°C for 6, 12, and 24 h. Following incubation, samples were transferred to sterile water and subjected to ultrasonication to detach adherent bacteria. The resulting bacterial suspensions were serially diluted, plated on agar plates, and incubated at 37°C for 24 h for colony counting. The antibacterial efficacy was calculated by comparing the colony-forming units (CFU) between test and control groups.

2.6.2. Bacteria stained alive and dead

Bacterial viability was evaluated by inoculating 100 μL bacterial suspension onto samples (37°C, 24h). After sonication in sterile water, bacteria were collected by centrifugation (10,000×g, 5min), washed with PBS, and resuspended (~10^8 cells/mL). The suspension was stained with SYTO 9/PI (manufacturer's ratio, 37°C, 15min dark), then visualized by fluorescence microscopy (SYTO 9: 503/530 nm for live cells; PI: 535/617 nm for dead cells).

2.6.3. Antibacterial stability

Antibacterial stability followed the same bacterial preparation. UV-sterilized samples were pre-immersed in PBS (1 mL/well) at 37°C for 3-7 days before bacterial challenge. For each time point, 50 μL bacterial suspension was applied to samples and incubated for 24 h. Adhered bacteria were then sonicated off, plated, and counted after 24 h culture.

2.7. In vivo animal study

This study was conducted using healthy Sprague-Dawley rats aged 8-12 weeks (body weight 200-300 g). All the animal operations and experiments were approved by the Institutional Animal Care and Use Committee of Peking University Shenzhen Hospital (ethical approval No.2022-164). The animals were randomly assigned to three experimental groups: (1) control group (bone defect only), (2) infection group (bone defect with *Staphylococcus aureus* inoculation), and (3) treatment group (implant samples in the bone defect bacterial infection model). Surgical procedures were performed through a longitudinal lateral incision on the hind limb to expose the femoral midshaft. A 3 mm full-thickness critical-sized bone defect was created using a low-speed electric drill. In both infection and treatment groups, the defect site was inoculated with 1×10^6 CFU of *S. aureus* suspension prepared in phosphate-buffered saline (PBS). The treatment group simultaneously received magnesium alloy implantation at the defect site. Acute inflammatory responses were evaluated at 7 days post-operation. After 8 weeks, bone regeneration was quantitatively assessed by micro-computed tomography (micro-CT) to measure the defect area, new bone volume (BV/TV), and bone mineral density (BMD). Micro-CT scans were reconstructed and analyzed using CTAn software (Bruker). BMD was calibrated using a hydroxyapatite phantom; BV/TV is the ratio of bone volume to tissue volume; Tb.Sp denotes trabecular separation; BS/BV is the bone surface-to-bone volume ratio. All parameters were calculated according to international standard definitions. Histopathological evaluation was performed using hematoxylin and eosin (H&E) staining to examine inflammatory cell infiltration and pathological changes in bone tissue at the implantation site. All statistical analyses were performed using SPSS 22.0 software (IBM Corp.). Intergroup comparisons were conducted using one-way analysis of variance (ANOVA), with a p-value <0.05 considered statistically significant (see Fig. 1).

3. Results

3.1. Coating characterization

The surface morphologies of AZ31, PEO, PEO-P@I, and PEO-P@I-A, as observed by SEM and elemental mapping via EDS, are presented in Fig. 2. The surface of AZ31 exhibits a scratch morphology resulting from polishing, with the main detected element being Mg (93.3%), with a minor amount of O (6.7%), which primarily originates from the natural oxidation of the Mg alloy. The PEO specimen exhibits a typical porous morphology produced by intensive discharge and entrapped gas. The micro-pores present an uneven size distribution, with diameters ranging from approximately 0.5 μm to 5 μm and an average diameter of 1.8 ± 0.6 μm (mean ± SD, n = 50 pores measured from multiple SEM images). The EDS scan indicates that the PEO layer is primarily composed of Mg (32.4%), O (57.5%), and P (10.1%, originating from the electrolyte). A relatively flat and uniform polymer-coating morphology is produced by the PEO-P@I surface because of loading the ICA/PTMC coating, obscuring the porous morphology of the PEO layer. The EDS results prove that the coating consists of C (73.2%) and O (26.2%), mainly originating from PTMC and ICA. The PEO-P@I-A surface shows a significant increase in N (9%) as detected by surface EDS, indicating successful grafting with AMPs. In contrast, the cross-sectional EDS results showed no detectable N. This discrepancy is attributed to the fact that AMPs are grafted as an ultrathin molecular layer (likely a few nanometers thick) on the outermost surface, which is below the detection sensitivity of cross-sectional EDS analysis but readily detectable by surface-sensitive techniques such as XPS.

The cross-sectional morphologies and EDS mappings of the coatings are presented in Fig. 3. The cross-section of the PEO layer shows

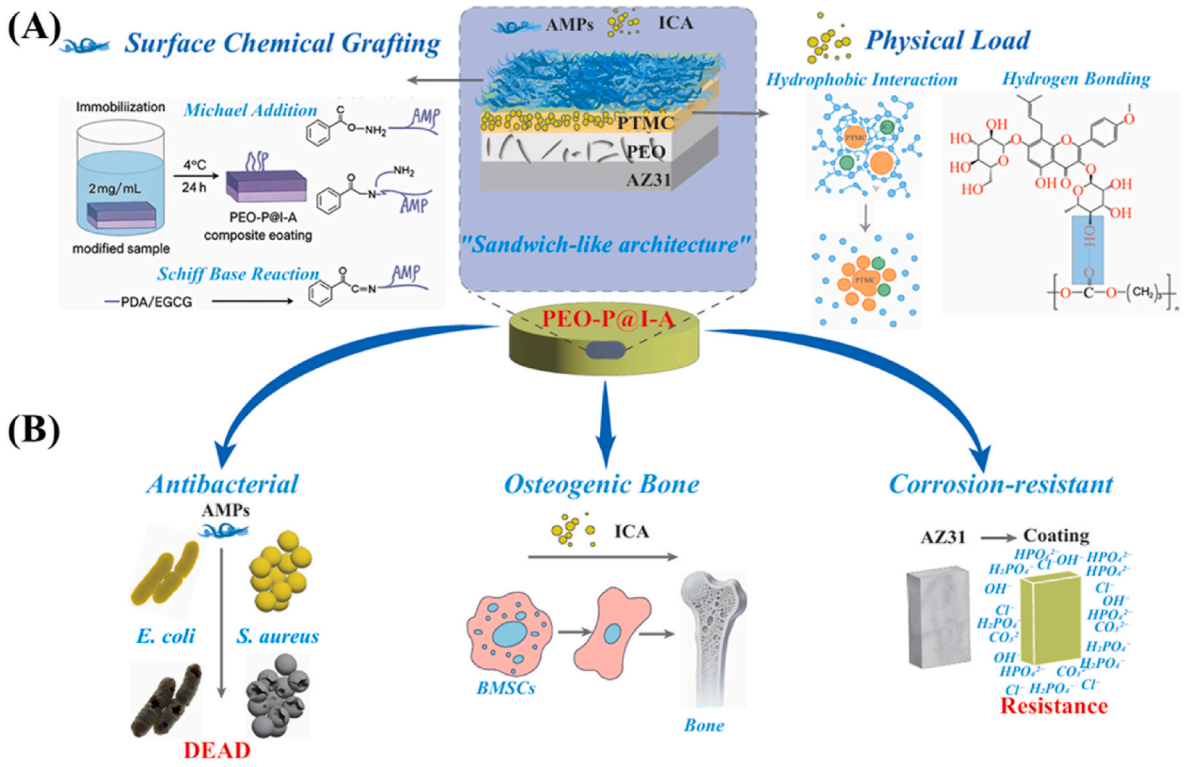


Fig. 1. (A) Schematic illustration of the coating construction and (B) evaluation of anti-corrosion, osteogenesis and antibacterial properties.

discharge channels and open pores with an average thickness of approximately 5.6 μm, and EDS confirms the presence of Mg, O, and P. In contrast, the cross-section of PEO-P@I exhibits a uniformly coated polymer coating with an approximate thickness of 45.8 μm on the PEO layer surface.

The XRD peak image of the PEO layer is displayed in Fig. 4A. The primary phase of the PEO layer contains MgO in addition to the peaks of Mg. The diffraction peak of magnesium phosphate is absent, and may be existing in an amorphous state. FT-IR analysis is performed, and the results are compared with that of the AZ31 control group, as shown in Fig. 4B. A broad peak observed at 1000-1300 cm^{-1} on the PEO is attributed to the absorption peaks of P═O (phosphoryl group) and P–O (phosphorus-oxygen bond), suggesting that the PEO layer contains compounds such as magnesium phosphate. After the deposition of the ICA/PTMC coating, broad peaks emerge at 3400 cm^{-1} on the surfaces of PEO-P@I and PEO-P@I-A, which may originate from the phenolic hydroxyl groups (O–H) in the ICA structure and/or the primary amine groups (N–H) in the AMP structure [62]. The $–CH_2$ stretching vibration peaks at 2980 and 2910 cm^{-1}, –COOR C═O stretching vibration peak at 1740 cm^{-1}, and C–C stretching vibration peak at 1480 cm^{-1} predominantly originate from the PTMC. The absorption peaks between 1500 and 1600 cm^{-1} correspond to the benzene-ring skeleton vibration peaks of the ICA structure [63]. The -amide I (-C═O stretching vibration) and -amide II (-NH deformation vibration and C–N stretching vibration) characteristic peaks are observed at 1630 and 1550 cm^{-1}, respectively, on the surface of PEO-P@I-A, indicating the successful grafting of AMPs.

The wettability of the samples was characterized using static water-contact-angle testing, as shown in Fig. 4C. The water contact angle of the bare AZ31 is 102.6 ± 1.7°, demonstrating typical hydrophobic characteristics. In contrast, the water contact angle of the PEO significantly decreases to 42.6 ± 1.1°. This notable alteration in wetting properties is primarily attributed to the porous structure formed during the PEO process, which increases surface roughness, thereby enhancing the surface's adsorption capacity for water molecules. The water contact angle of PEO-P@I increases to 70.2 ± 1.4°, due to the presence of PTMC, a hydrophobic polymer, which covers the PEO porous structure and renders the sample surface relatively hydrophobic. After further grafting with AMPs, the surface hydrophilicity increases, and the water contact angle decreases to approximately 46.3 ± 0.7. The change is attributed to the amino hydrophilic groups introduced by the AMPs.

The X-ray photoelectron spectroscopic (XPS) analysis of all the specimens are presented in Fig. 5. From the XPS full spectrum (Fig. 5A) and XPS atomic percentage (Table 2), the peak of P is detected on the surface of the PEO sample (9.81%), and the percentage content of O increases, compared to that of AZ31, suggesting the presence of a ceramic oxide layer containing P and O on the surface. The content of C on the surface of PEO-P@I increases significantly, while the content of Mg decreases. This is because of the PEO surface being covered by the PTMC coating loaded with ICA, both PTMC and ICA contain a large amount of C. After grafting AMPs, N is detected on the surface of PEO-P@I-A (6.06%). The results of a high-resolution fitting analysis of C 1s, O 1s, and N 1s on the surfaces of the PEO-P@I and PEO-P@I-A samples is presented in Fig. 5E–I. The C element (C 1s) in the two groups of samples may exhibit the following four bonding states: the aliphatic C–C at a binding energy of 284.6 eV; the aliphatic C–O at a binding energy of 287 eV; C═O at a binding energy of 288.1 eV; and O–C═O at a binding energy of 290.1 eV. The O element (O 1s) of the two groups of samples may have the following three bonding states: aromatic C–OH at a binding energy of 533.7 eV; O═C–O at a binding energy of 532.4 eV; and O═C–O at a binding energy of 531.6 eV. The detection of these bonding forms indicates that a PTMC coating loaded with ICA is deposited on the surface of PEO-P@I and PEO-P@I-A samples. It is noteworthy that N is detected on the surface of the PEO-P@I-A sample, and the high-resolution fitting result of N 1s (Fig. 5G) shows that it may have two bonding states: N–H with a binding energy of 399.4 eV and C–N with a binding energy of 401.3 eV. This result further confirms that the AMPs have been successfully grafted on the surface.

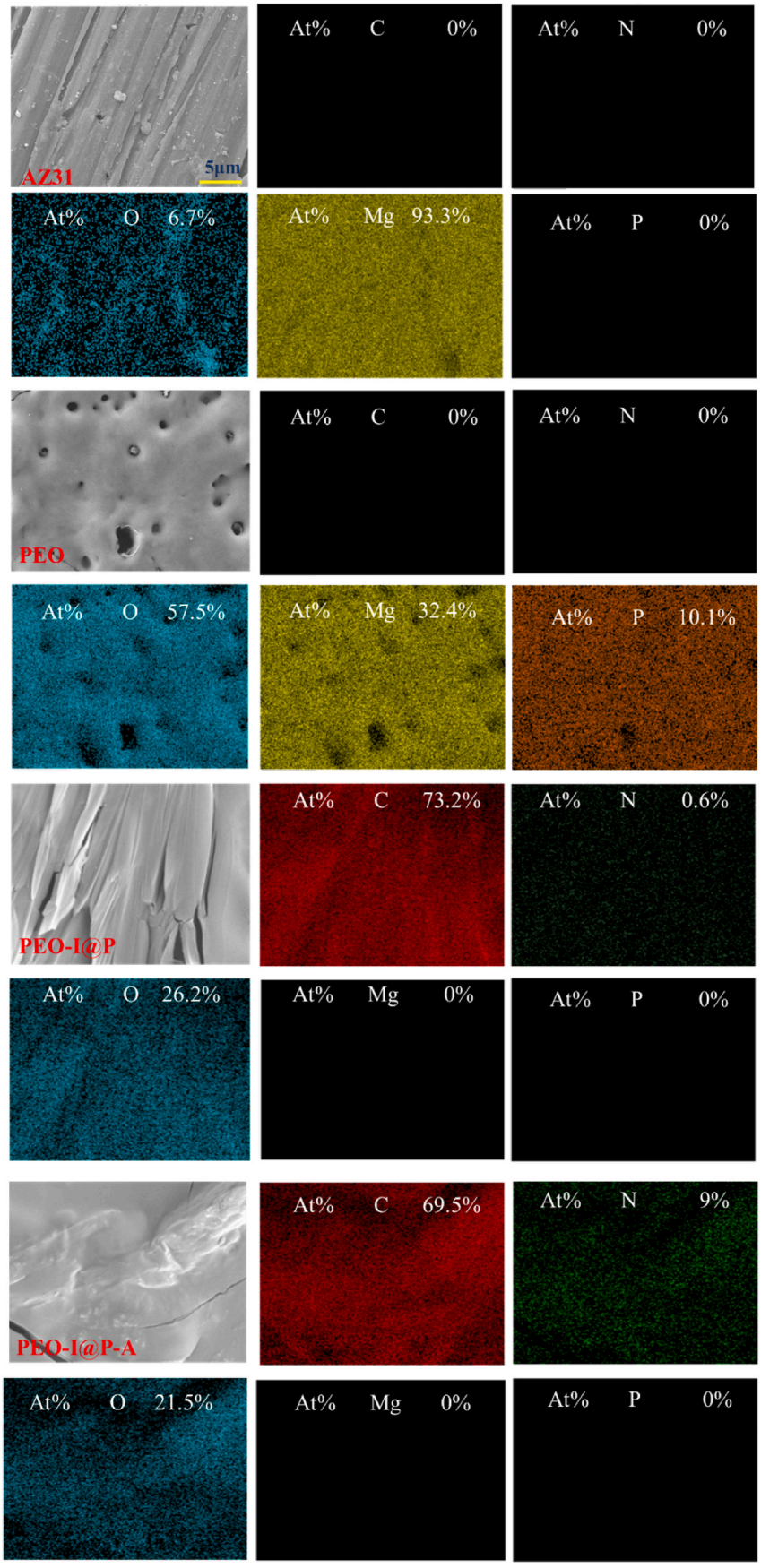


Fig. 2. Surface morphology and EDS mappings of AZ31, PEO, PEO-P@I and PEO-P@I-A coatings.

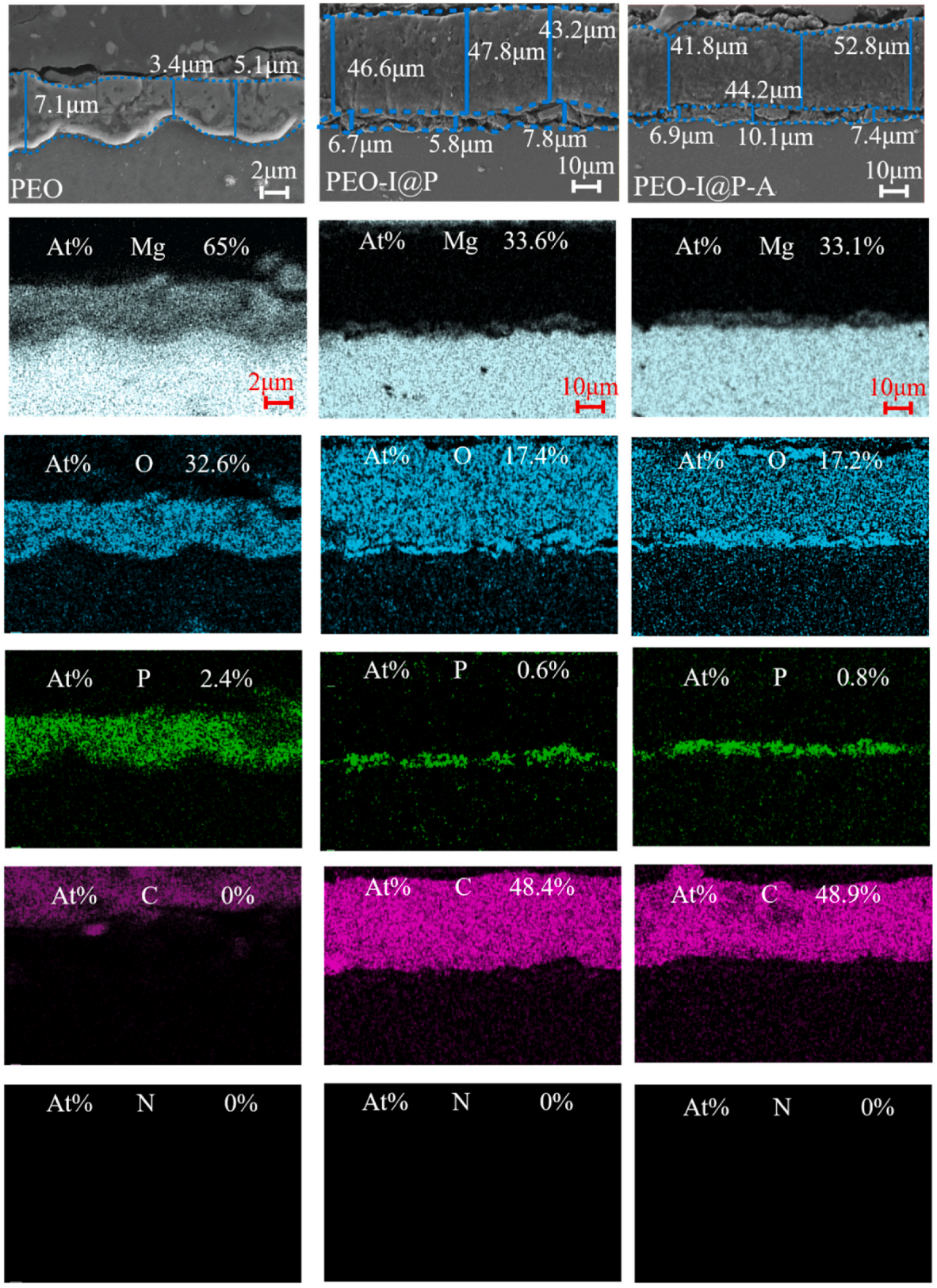


Fig. 3. Cross sectional morphology and EDS mappings of AZ31,PEO,PEO-P@I and PEO-P@I-A coatings.

3.2. Corrosion behaviours

The corrosion behaviours of the specimens in the SBF solution are evaluated using electrochemical and immersion tests. The polarization curves are depicted in Fig. 6A. The corresponding corrosion potential (E_{corr}) and corrosion current (i_{corr}), calculated by the Tafel extrapolation method, are listed in Table 3. The corrosion potential indicates the tendency of the corrosion reaction. The i_{corr} of AZ31 is $(2.57 \pm 0.42) \times 10^{-5}$ A/cm^2. The i_{corr} of PEO decreases by approximately one order of magnitude, to approximately $(1.61 \pm 0.27) \times 10^{-6}$ A/cm^2. A single PEO

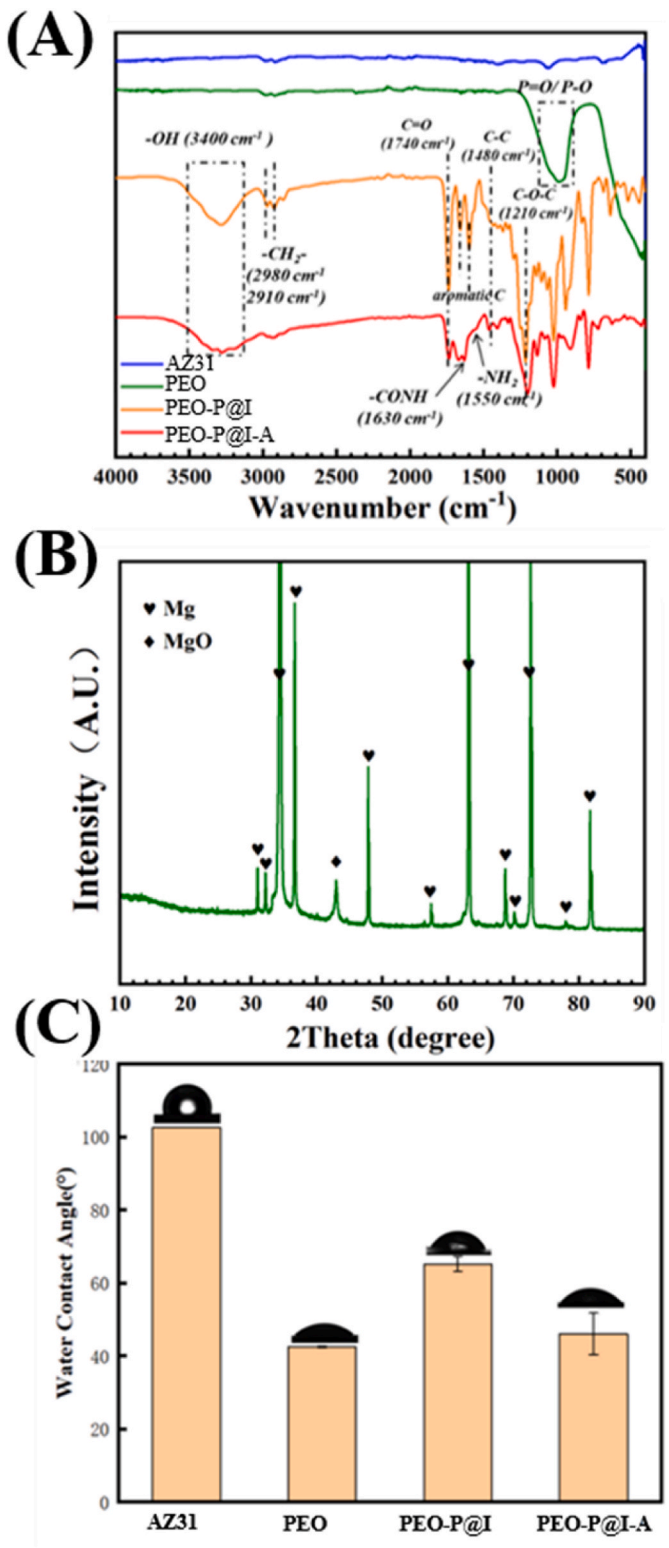


Fig. 4. Structural analysis of the respective coatings. (A)FT-IR spectra of Mg matrix and the coatings; (B)XRD pattern of PEO layer; (C)Water contact angles of AZ31 Mg and the coatings.

layer cannot effectively prevent the occurrence of corrosion, owing to its intrinsic porous structure. Owing to the excellent corrosion resistance of the PTMC coating, the i_{corr} of PEO-P@I and PEO-P@I-A further decrease remarkably, reaching $(1.96 \pm 0.31) \times 10^{-9}$ and $(1.54 \pm 0.22) \times 10^{-9}$ A/cm^2, respectively, with corrosion inhibition rates reaching 99.99%.

Fig. 6B–D display the electrochemical impedance spectra (EIS) of each sample, including Nyquist and Bode plots. In the EIS of AZ31, two capacitive arcs and one inductive arc are observed, while three capacitive arcs can be identified in the EIS of PEO, PEO-P@I, and PEO-P@I-A. The larger capacitive arcs of PEO-P@I and PEO-P@I-A signify that the coating possesses good corrosion resistance, as shown in Fig. 6B. In the |Z|–frequency Bode diagram (Fig. 6C), the low-frequency resistance of PEO is one order of magnitude higher than that of AZ31, and the low-frequency resistance of PEO-P@I and PEO-P@I-A are approximately three orders of magnitude higher than that of AZ31, indicating that the coating of PEO-P@I and PEO-P@I-A effectively enhances the corrosion resistance of the Mg substrate.

The time constants signify different physical characteristics for different treatments (Fig. 6D). For the AZ31 substrate, the one at high frequencies (10^2–10^5 Hz) are associated with the formation of corrosion products, while that at 10^{-1}–10 Hz represents the electrochemical responses of the electrical double layer between the corrosion products and Mg matrix. The low-frequency time constant is related to the corrosion reaction occurring at the interface. PEO displays two-time constants at medium–high frequencies (10–10^4 Hz), corresponding to the electrochemical responses of the outer and inner layers of the PEO layer. The time constants at low frequencies (10^{-2}–10 Hz) indicate the electrochemical responses of the electrical double layer between the PEO layer and Mg substrate. For PEO-P@I-A, the grafting of AMPs enhances the barrier performance, and AMPs did not form a separate layer in the cross-sectional morphology. Therefore, PEO-P@I and PEO-P@I-A both present three time constants. The time constant at high frequencies (10^3–10^5 Hz) represents the response of the composite structure, which combines the loaded ICA/PTMC layer and PTMC layer grafted with AMPs with the PEO porous outer layer in the system. The time constants at medium frequencies (10^1–10^3 Hz) can be attributed to the dense inner PEO layer, while the time constants at low frequencies (10^{-2}–10 Hz) indicate the electrical-double-layer response between the PEO layer and Mg substrate.

To further assess the corrosion stability of the coating, each group of samples is immersed in an SBF solution for 21 days. EIS tests are conducted on the 1st, 3rd, 5th, 7th, 14th, and 21st days, as depicted in Fig. 7. The time constants for all samples remain consistent throughout the immersion period. The impedance modulus of AZ31 initially decreases and then gradually increases. In the early stages of immersion, corrosion reactions cause the impedance modulus to drop; however, with the continuous deposition of corrosion products further corrosion reactions are partially hindered, leading to a gradual increase in the impedance modulus. Initially, the impedance modulus of PEO at low-frequency was approximately one order of magnitude higher than that of the Mg matrix. However, over the 14-day immersion period, the modulus continuously decreased to less than 10^3 Ω cm^2. Considering the degradability of the system, the thickness of the PEO pre-treatment layer used in this study is relatively thin. The corrosion medium penetrates the interior through micro-pores and discharge channels, resulting in degraded corrosion performance. Following the initial immersion stage, the low-frequency impedance modulus of the PEO-P@I and PEO-P@I-A increase by approximately three orders of magnitude. As the immersion time increases, the decreasing rate of impedance modulus slows, indicating that the composite coating significantly enhances the corrosion resistance. The PEO-P@I-A exhibits the highest impedance modulus capability. Despite the continuous penetration of the corrosive medium, which gradually reduced the impedance modulus, the low-frequency impedance modulus of PEO-P@I-A remained above 10^6 Ω cm^2 after 21 days of immersion.

The corroded morphology and corresponding local composition analysis are presented in Fig. 8. Numerous flocculent structures are detected on the surface of the Mg alloy, which are corrosion products mixed with a small amount of precipitated calcium phosphate phases. The same structure also appears on the PEO surface, suggesting the occurrence of similar chemical reactions. A few cracks are visible, which

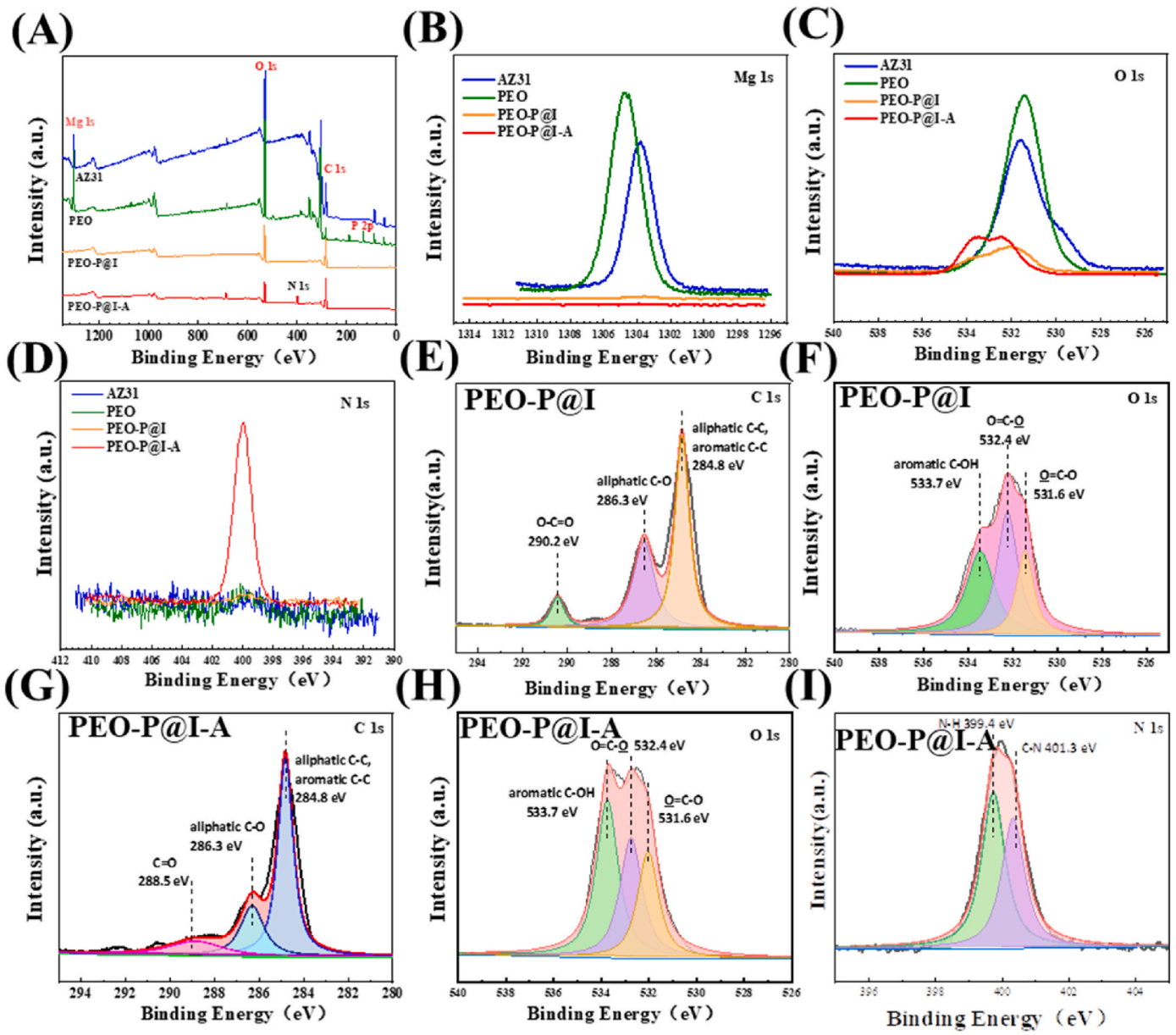


Fig. 5. XPS analysis of the Mg matrix and coatings High-resolution spectra of the (A) full XPS spectra; (B) Mg 1s, (C) O 1s, and (D) N 1s of each group; Fitting results of high-resolution spectra of C 1s (E) and O 1s (F) of PEO-P@I; Fitting results of high-resolution spectra of C 1s (G), O 1s (H), and N 1s (I) of PEO-P@I-A.

Table 2
XPS analysis of the surface elemental composition and atomic percentage of the specimens.

Specimen	C 1s	Mg 1s	O 1s	P 2p	N 1s
AZ31	45.95	12.96	40.38	0.6	0.11
PEO	17.64	19.01	52	10.81	0.54
PEO-P@I	65.75	2.74	29.75	1.27	0.49
PEO-P@I-A	64.3	2.35	26.25	1.04	6.06

may be caused by long-term soaking corrosion. A small number of lumpy structures are present on the surface of PEO-P@I, and EDS profiling results indicate that these precipitates consist of mixed compounds containing Ca, P, and Mg elements.

The reaction of Mg substrate with corrosive media results in an increase in the solution pH, hydrogen gas generation, and release of Mg ions, which reflects the corrosion resistance of the system. Long-term immersion tests involve monitoring changes in pH, hydrogen-evolution volume, and Mg-ion concentration. As depicted in Fig. 9. The total hydrogen-evolution volume for AZ31 is approximately 4.16 mL cm^{-2}, whereas that for PEO is approximately 1.50 mL cm^{-2} following a 21-day immersion. In comparison, the total hydrogen-evolution volumes for PEO-P@I and PEO-P@I-A are approximately 0.78 mL cm^{-2} and 0.75 mL cm^{-2}, respectively. Assessing the hydrogen-evolution rate of Mg-based implants is crucial, as excessively high rates can cause subcutaneous bubbles and inflammation [64–66]. The hydrogen-evolution rates are calculated and listed in Fig. 9A. The coated samples all exhibit markedly lower hydrogen-evolution rates, than the bare AZ31. The hydrogen evolution volumes of PEO-P@I (0.037 mL cm^{-2} day^{-1}) and PEO-P@I-A (0.036 mL cm^{-2} day^{-1}) were significantly lower than those of AZ31 (4.16 mL cm^{-2} day^{-1}) and PEO (1.02 mL cm^{-2} day^{-1}) at 21 days as depicted in Fig. 9B. Research has indicated that in mice, a hydrogen-evolution rate of 0.068 mL cm^{-2} day^{-1} is tolerable [67].

As illustrated in Fig. 9C, AZ31 exhibits the largest pH variation throughout the immersion period, increasing to approximately 9.3 by

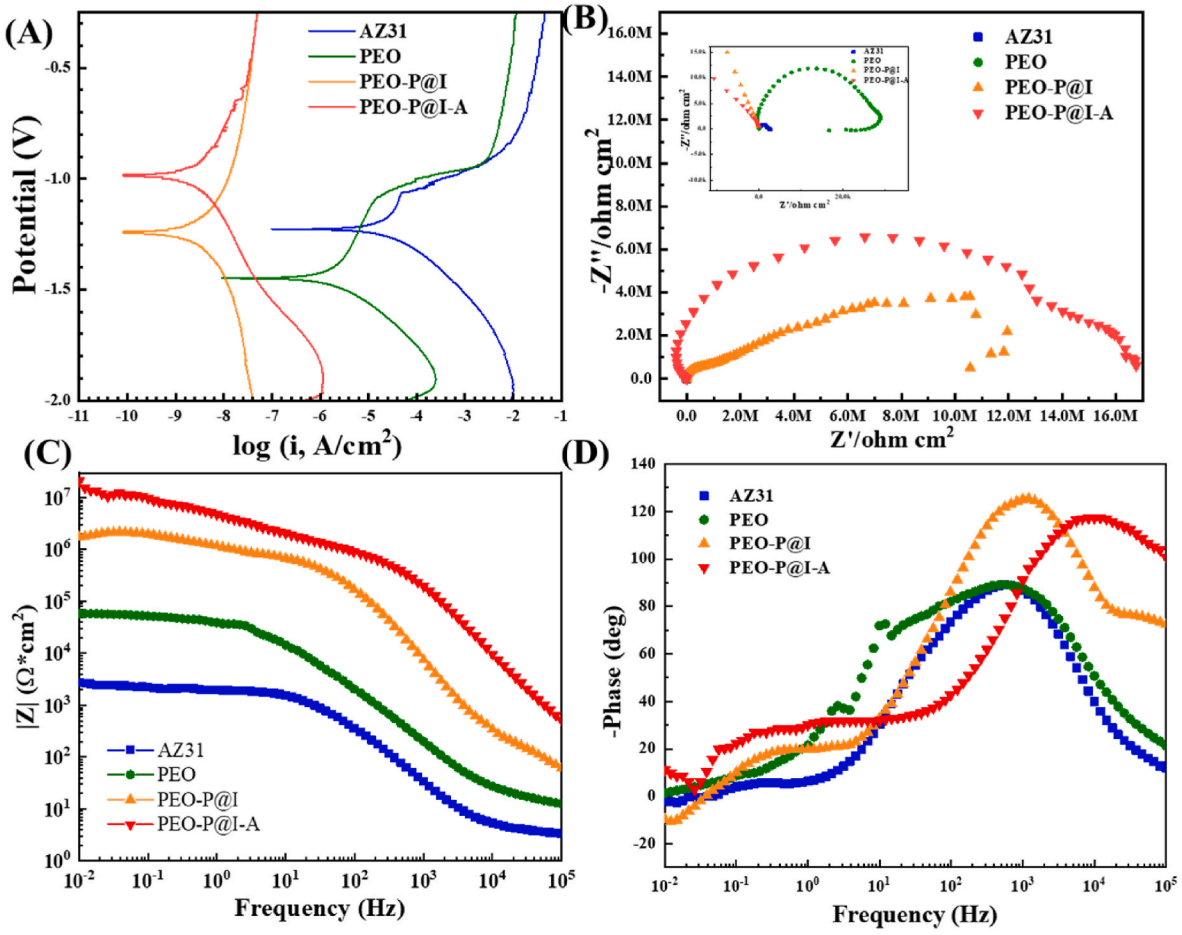


Fig. 6. (A)Potentiodynamic polarization curves; (B)Nyquist plots; (C)|Z| plots; (D)Phase angle of the AZ31 alloy and coatings.

Table 3
Calculated results originated from the polarization curves via Tafel extrapolation.

Specimen	E_{corr} (VSCE)	i_{corr} (A/cm^2)	η (%)
AZ31	−1.23 ± 0.1	(2.57 ± 0.42)×10^{-5}	0
PEO	−1.45 ± 0.3	(1.61 ± 0.27)×10^{-6}	93.73
PEO-P@I	−1.53 ± 0.2	(1.96 ± 0.31)×10^{-9}	99.99
PEO-P@I-A	−1.24 ± 0.1	(1.54 ± 0.22)×10^{-9}	99.99

day 21. In coated samples, PEO showed significantly smaller pH changes than AZ31 during the first 10 days of immersion. The coating partially blocked substrate–solution contact, slowing corrosion. After 10 days, pH rose to levels similar to AZ31. Despite its dense inner layer, corrosive media penetrated through pores to the interface, causing localized corrosion and coating failure, leading to a sharp increase in pH. In contrast, PEO-P@I and PEO-P@I-A maintain stable pH values around 7.5 throughout the 21-day immersion, primarily attributed to the protective PTMC coating covering these samples. The hydrophobic PTMC layer exhibits surface erosion degradation and demonstrates superior corrosion resistance.

The samples AZ31, PEO, and PEO-P@I-A are immersed in PBS solution at a surface area/volume ratio of 0.05 cm^2/mL. The Mg-ion concentration in the solution is measured every three days, as shown in Fig. 9D. The total Mg-ion release of AZ31 is approximately 75.93 mg/mL after 21 days of immersion, that of PEO is approximately 76.33 mg/mL, and that of PEO-P@I-A is approximately 36.1 mg/mL. Magnesium ion release meets the maximum safe concentration in the body of 200 mg/mL [68–70]. The total magnesium ion release of PEO is close to that of AZ31, indicating that the long-term protective performance of the PEO layer is insufficient. The magnesium ion release concentration of PEO-P@I-A is significantly reduced. AZ31 releases Mg ions rapidly upon contact with PBS solution, but the rate slows as corrosion products deposit on the surface. After 6 days, AZ31's Mg-ion concentration reaches about 24.07 mg/mL, while PEO's is lower at 14.77 mg/mL, indicating initial corrosion inhibition by the PEO layer. With prolonged immersion, PEO's release increases significantly, likely due to PBS penetration through pores or defects at the coating-substrate interface, triggering substrate corrosion and Mg-ion release from PEO degradation. In contrast, PEO-P@I-A exhibits a stable release trend, with Mg-ion concentrations around 5 mg/mL, demonstrating consistent and durable protection.

3.3. Icariin released in vitro

The in vitro release results of PEO-P@I-A samples in PBS buffer were measured using a UV spectrophotometer at 37 ± 1.0°C, as shown in Fig. 10. The results indicate that ICA was released steadily over 14 days, with a maximum average release of 64.31 μM. Fig. 10B shows that ICA exhibited higher release concentrations in the early soaking period (1-5 days), while in the later soaking period (5-14 days), the coating released steadily, maintaining a concentration of 7-10 μM.

3.4. Biological evaluation

3.4.1. BMSC cells compatibility

The cytotoxicity evaluation of the samples on BMSC cells

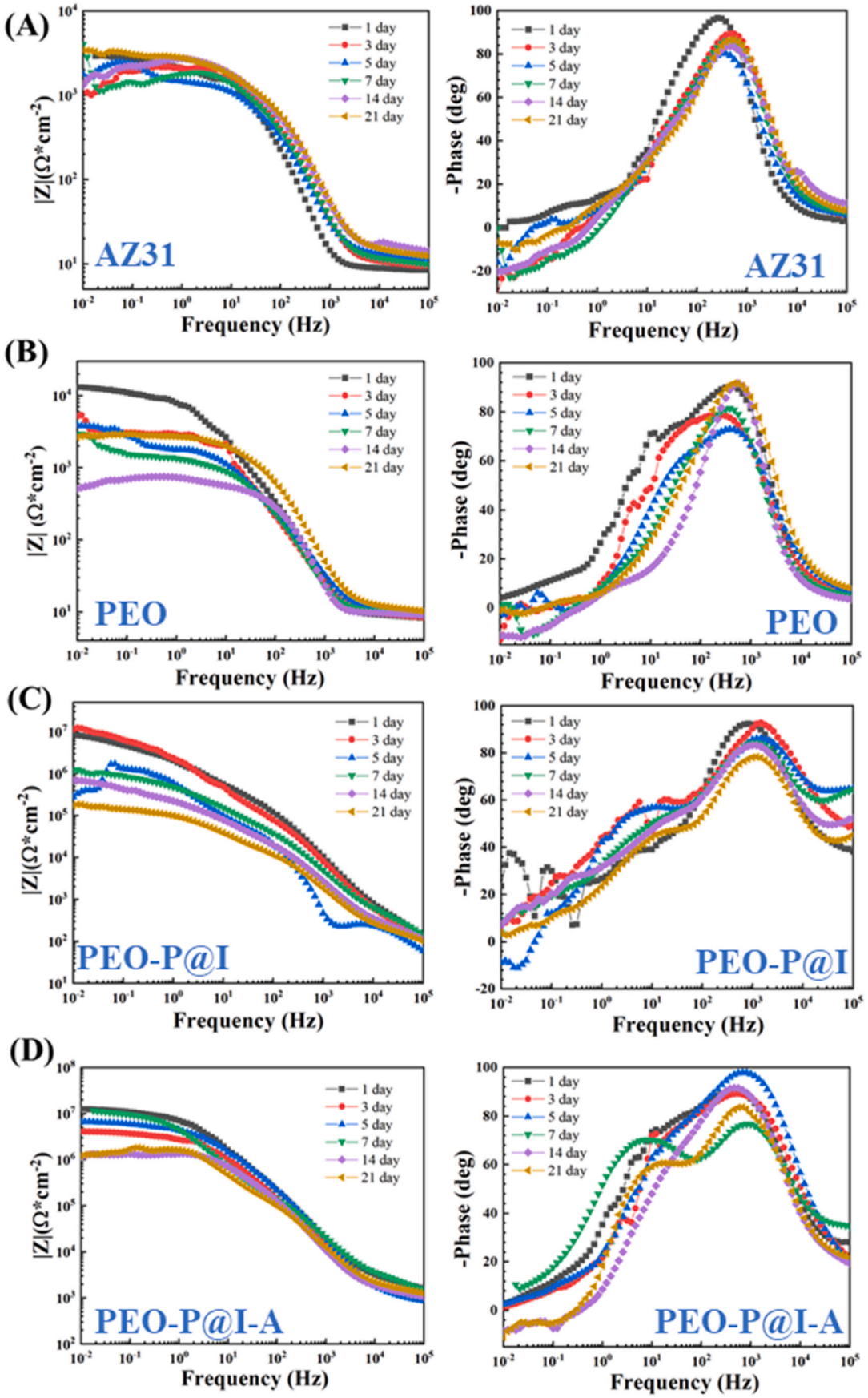


Fig. 7. EIS spectra of the specimens recorded in SBF at 37°C within 21 days (A)AZ31; (B) PEO; (C) PEO-P@I; (D) PEO-P@I-A.

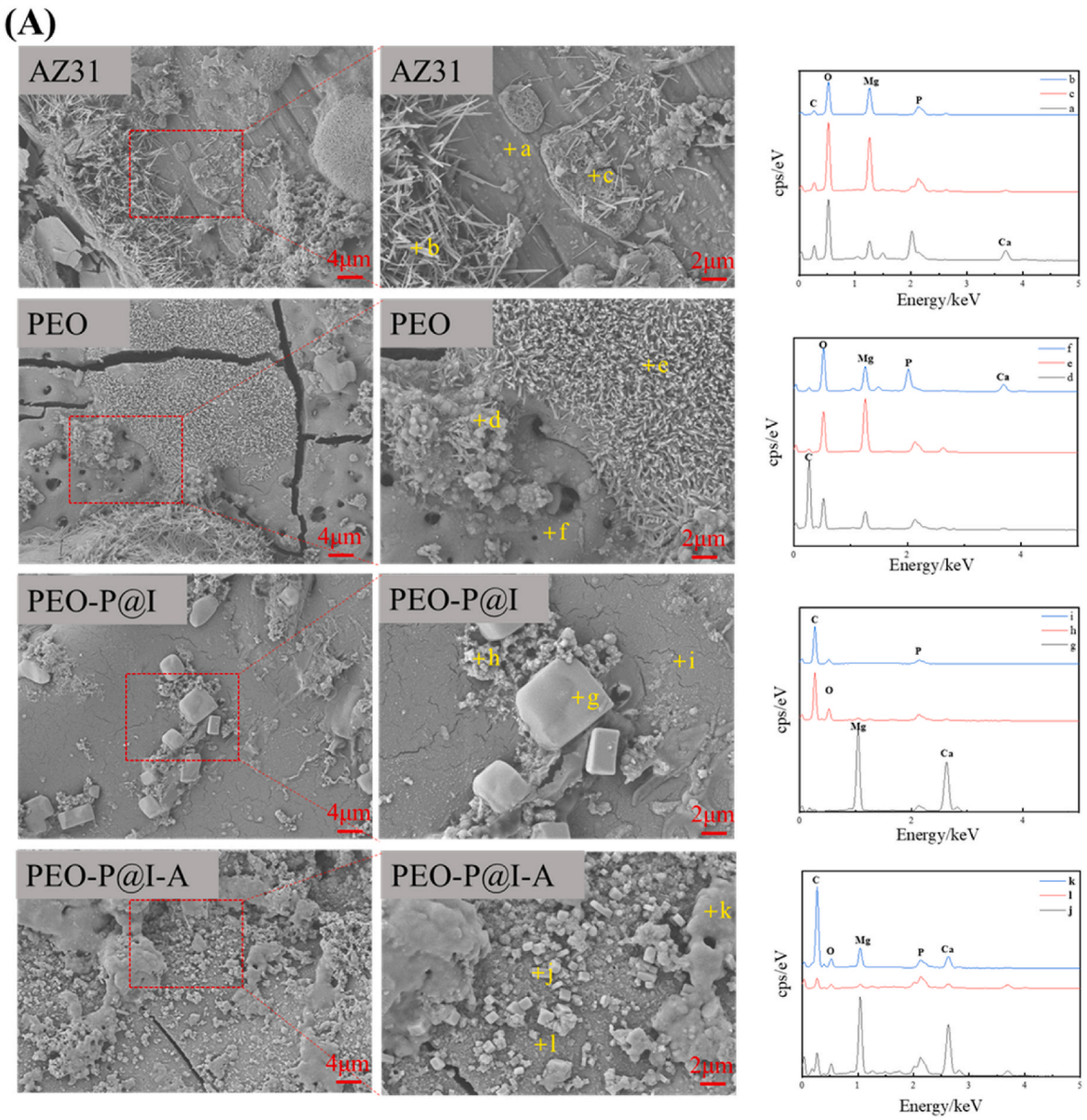


Fig. 8. (A)Surface morphology and EDS mappings of AZ31 AZ31, PEO, PEO-P@I and PEO-P@I-A coatings of samples during the 21-day immersion in the SBF solution at 37 ± 0.5°C.

(Fig. 11A–D) demonstrates that the relative cell viability exceeds 75% at an extract concentration of 25%. Notably, both the PEO-P@I and PEO-P@I-A exhibit excellent cytocompatibility across all tested concentrations, consistently maintaining the cell viability above 75%. To further assess the biocompatibility of the composite coatings, BMSC cell growth is examined using live/dead cell staining (Fig. 11E). After 3 and 5 days of culture, all experimental groups show only minimal dead cells, while the control group exhibits relatively lower cell density at both time points. These results indicate that the composite coatings possess favorable biosafety towards cells. All data shown were obtained using 25% material extracts.

The osteogenic potential of the samples is evaluated in-vitro, with results presented in Fig. 11F. ALP staining after 7 days of culture reveal markedly darker brown coloration, compared to the control group. Quantitative analysis demonstrates that the area of darker brown nodules on the PEO-P@I and PEO-P@I-A coatings increased by 35–40%, relative to that on the control, and by 25–30% compared to that on the AZ31 group. BMSCs were cultured with 25% sample extracts for 21 days, and the in vitro biomineralization ability was evaluated by alizarin red S (ARS) staining. The area of mineralized calcium nodules in PEO-P@I and PEO-P@I-A groups increased by 40%–50% compared with the control group, and by 65%–70% compared with the PEO group. Meanwhile, the introduction of AMPs had almost no effect on the osteogenic induction and mineralization of ICA.

The mRNA was extracted from the cultured BMSC cells and analyzed by quantitative real-time PCR (qPCR), with a focus on the expression levels of key genes (ALP, Runx2, OPN, Col-I) related to osteoblast differentiation, as shown in Fig. 12G. The results demonstrate that the ALP expression levels in both the PEO-P@I and PEO-P@I-A groups are significantly upregulated by 2.6 ± 0.2 fold, compared to that of the control group ($p < 0.01$). This indicates that ICA promotes early osteogenic differentiation and enhances alkaline phosphatase activity, facilitating the initiation of extracellular matrix mineralization. Runx2 expression reached 1.7 ± 0.1-fold that of the control ($p < 0.05$), suggesting that ICA may drive osteogenic differentiation by activating Runx2 transcriptional activity. The expression of the mid-to-late-stage

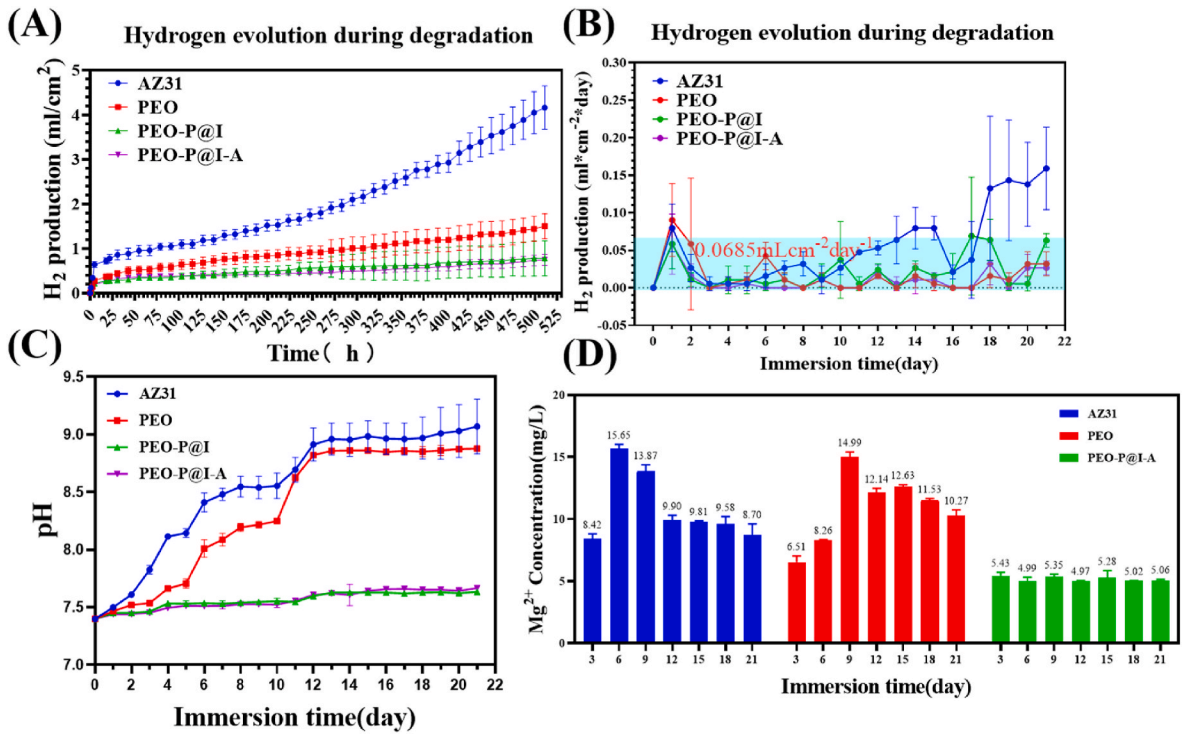


Fig. 9. (A) Hydrogen evolution; (B) hydrogen release rate; (C) pH changes of each group of samples during the 21-day immersion in the SBF solution at 37 ± 0.5°C; (D) The released magnesium concentration of AZ31, PEO and PEO-P@I-A within 21 days of immersion in s in PBS solution at 37 ± 0.5°C.

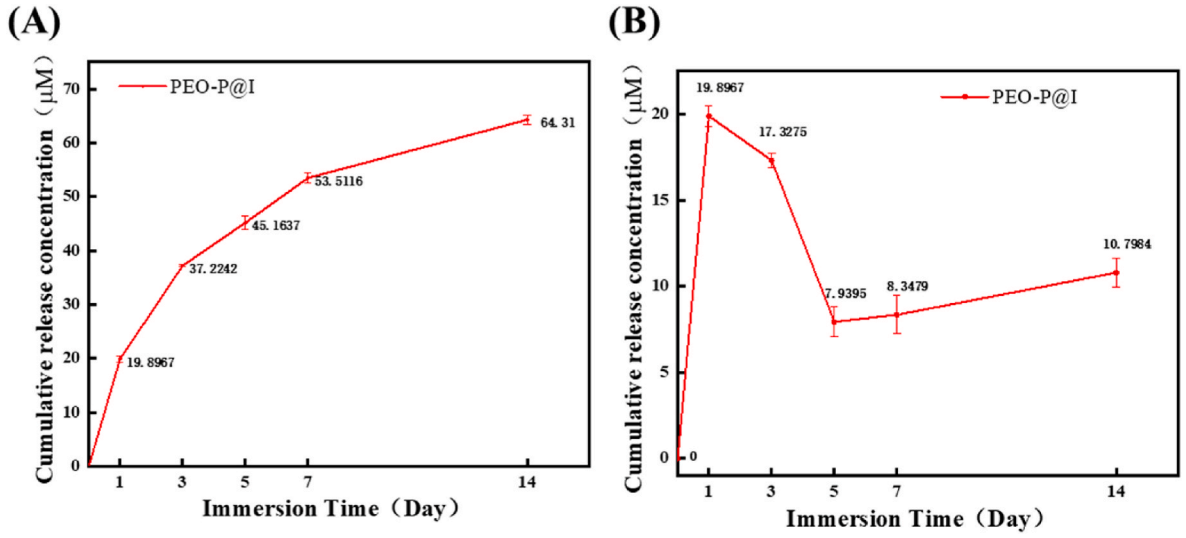
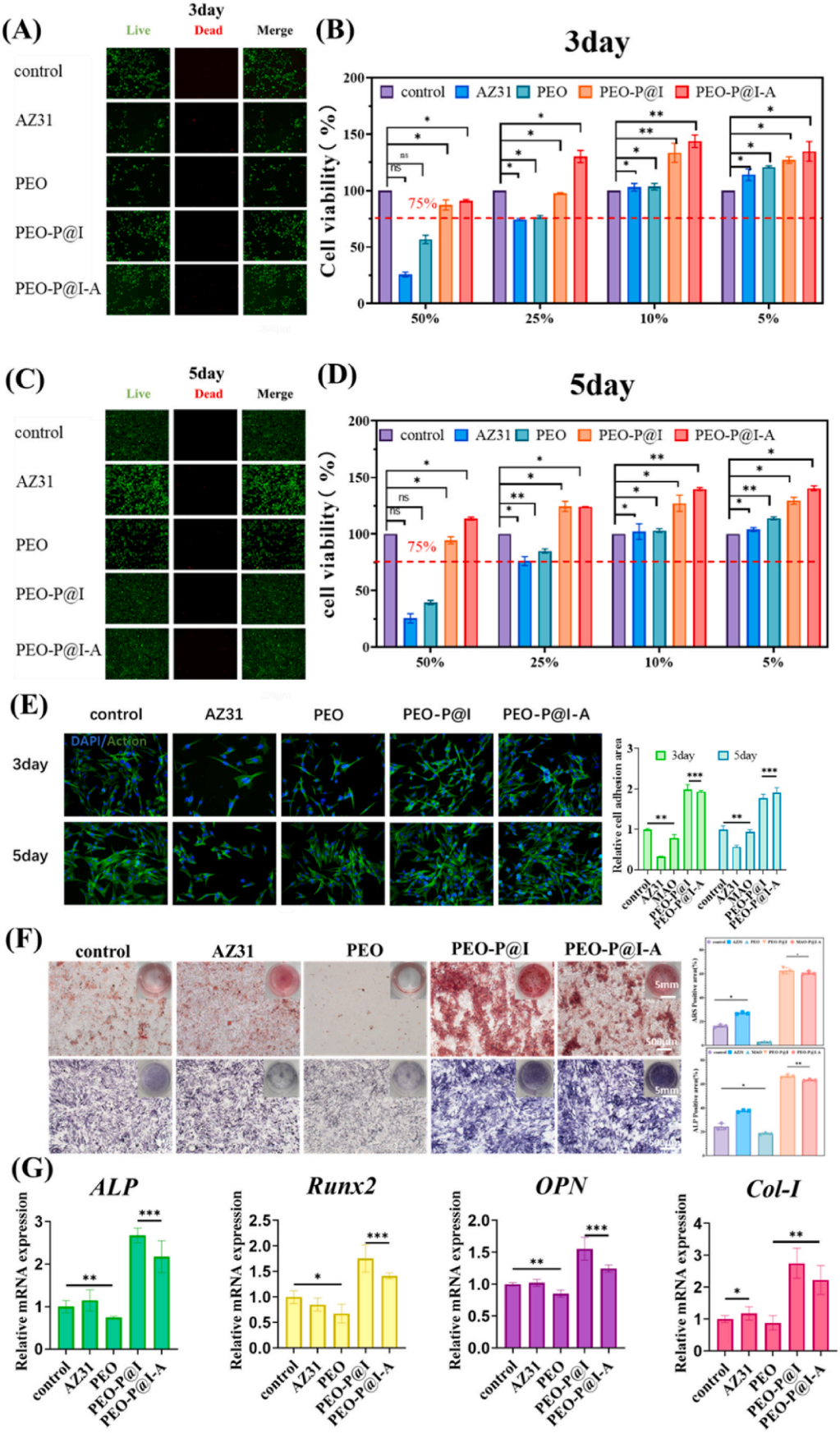


Fig. 10. (A) ICA cumulative release concentration and (B) Release concentration the 14-day immersion of samples in PBS solution.

marker OPN is upregulated by 1.5 ± 0.2-fold ($p = 0.05$), potentially associated with the extracellular matrix maturation and mineralization processes. ICA significantly stimulates Col-I synthesis (2.7 ± 0.3-fold increase, $p < 0.01$), indicating its efficacy in promoting collagen deposition to provide structural support for bone-matrix formation. Collectively, ICA markedly upregulates the expression of osteogenesis-related genes, with particularly pronounced effects on OPN and Col-I, demonstrating considerable potential to promote osteogenic differentiation.

To investigate the impact of composite coatings on ferroptosis, BMSC cells are first cultured and pre-treated with ferric ammonium citrate (FAC) in 24 h coating extracts, followed by Prussian blue staining (Fig. 12A). Compared to the positive control (FAC-treated) group, cells treated with PEO-P@I and PEO-P@I-A extracts exhibit a significant reduction (approximately 70–85%) in the number of deep-blue granules, as well as decreased staining area and intensity. The diffuse or clustered distribution of deep-blue granules observed in the positive control is markedly attenuated in the treatment groups. ICA may suppress ferroptosis-related pathways through modulation of iron metabolism and key gene expression. Further qPCR analysis of key ferroptosis regulatory genes (GPX4, SLC7A11, TFR1, ACSL4) (Fig. 12B) reveals that ICA treatment significantly upregulates GPX4 (4.0 ± 0.1-fold, $p < 0.01$) and SLC7A11 (4.0 ± 0.3-fold, $p < 0.05$) expression, while significantly downregulating TFR1 (0.41 ± 0.01-fold, $p < 0.01$) and ACSL4 (0.44 ± 0.01-fold, $p < 0.01$) expression levels. However, direct evidence of lipid peroxidation is still needed for confirmation.



(caption on next page)

Fig. 11. In vitro cytocompatibility of AZ31, PEO, PEO-P@I and PEO-P@I-A extract culture with BMSCs. (A) and (C) Live (green)/dead (red) staining of BMSCs after 3 and 5 days of incubation. (B) and (D) Cell viability; (E) FITC (green)/DAPI (blue) staining of BMSCs after 3 and 5 days of incubation and quantitative data of cell adhesion number; (F) ALP and alizarin red staining and quantification; (G)The qPCR results for the relative mRNA expression of angiogenesis-related genes, including ALP, Runx2, OPN, and Col-I after 7 days of incubation.

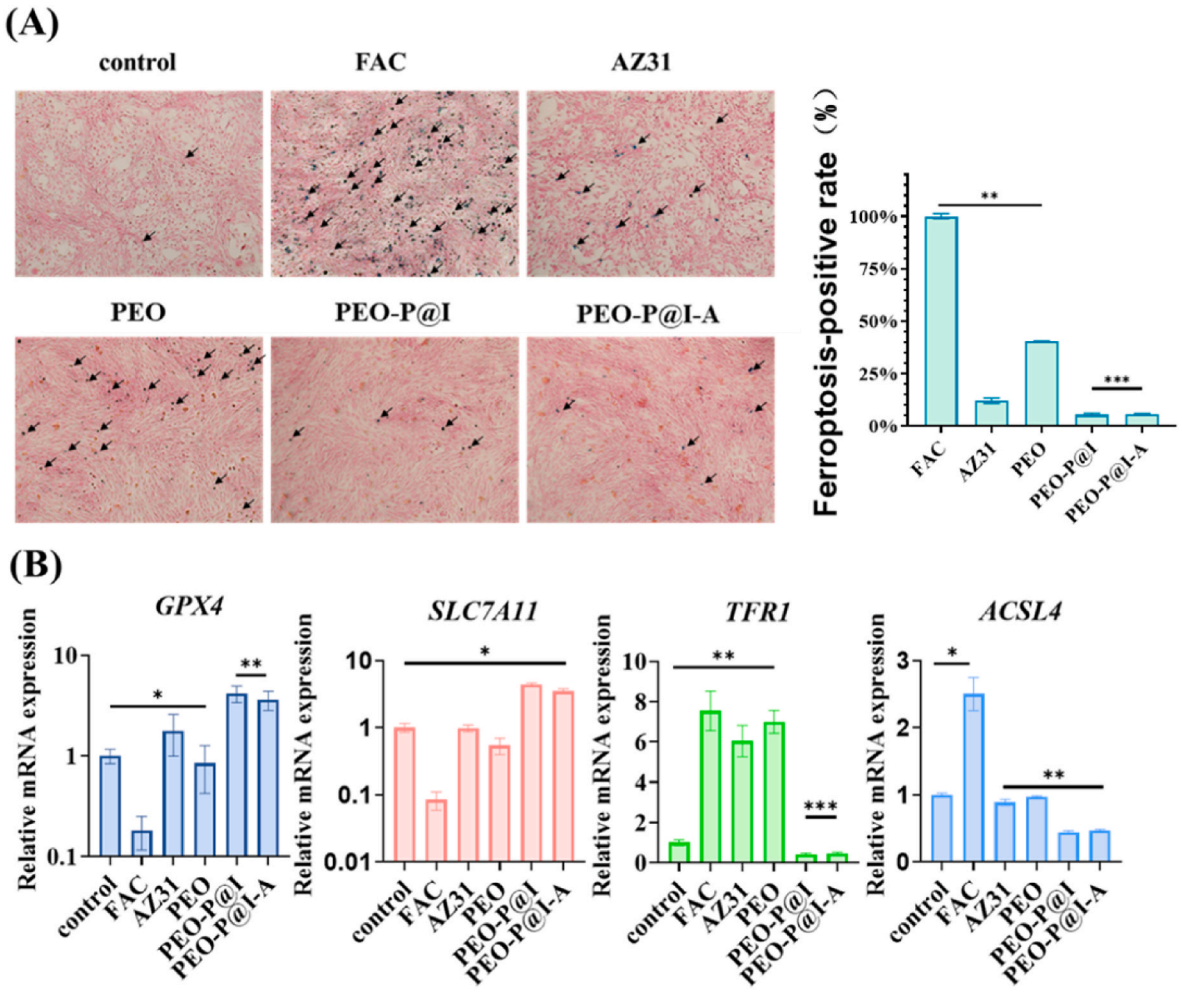


Fig. 12. (A) BMSCs Cell Prussian blue dyeing after 7 days of incubation; (B) The qPCR results for the relative mRNA expression of angiogenesis-related genes, including GPX4, SLC7A11, TFR1, and ACSL4 after 7 days of incubation.

3.4.2. HUVECs cell compatibility

Bone is a highly vascularized tissue, and the long-term survival of an implant fundamentally depends on its ability to establish an effective blood supply with the host. In order to evaluate the ability of this coating to guide angiogenesis, the function of endothelial cells was evaluated (Fig. 13A). The HUVECs cell viability remains above 75% when the sample extracts are diluted to a concentration of 25%, and it was consequently established as the standard concentration for subsequent experiments. Analysis via live/dead fluorescence staining (Fig. 13B) and cytoskeletal staining (phalloidin staining, Fig. 13C) reveal that, compared to the AZ31 and PEO groups, both the PEO-P@I and PEO-P@I-A groups exhibit significantly enhanced cell viability during the 3 and 5-day culture periods. This is evidenced by a 35–45% increase in the fluorescence intensity and a concurrent significant increase in the cell number (reflected by a 1.3 ± 0.1-fold increase in the fluorescent cell area, $p < 0.01$). Furthermore, cell-migration assays (Fig. 13D) confirm that treatment with the composite coatings for 12 h results in a 35–40% enhancement in HUVECs cell-migration rate. Collectively, the PEO-P@I and PEO-P@I-A possess the potential to promote angiogenesis by significantly enhancing the endothelial cell viability and promoting cell proliferation and migration capabilities.

3.4.3. Macrophages compatibility

The cytocompatibility of the samples with RAW264.7 macrophages and their immunomodulatory effects on inflammation were systematically evaluated, as shown in Fig. 14. Cytotoxicity assessment using the CCK-8 assay (Fig. 14A) reveals that the cell viability remains above 75% when the extract dilution concentration is 25%. Notably, both the PEO-P@I and PEO-P@I-A groups maintain cell viability exceeding 75%, across all tested concentrations, indicating favorable cytocompatibility of these composite materials. Live/dead fluorescence staining analysis (Fig. 14B) and cytoskeletal staining (phalloidin staining, Fig. 14C) showed that the PEO-P@I and PEO-P@I-A groups exhibited significantly enhanced cell viability compared to the AZ31 and PEO groups during both 3-day and 5-day culture periods. Fluorescence intensity increased by 40-42% and cell numbers increased significantly at the same time (fluorescent cell area increased by 1.1 ± 0.05-fold, $p < 0.01$). To further investigate the regulatory mechanism of the composite coatings on macrophage inflammation, we analyse the expression changes of key inflammatory cytokines using qPCR (Fig. 14D). The results demonstrate that the composite coating significantly suppress the expression of pro-inflammatory cytokines: compared to the control group, IL-6 expression decreases by 3.5 ± 0.8-fold ($p < 0.01$). Suppression of IL-12 expression

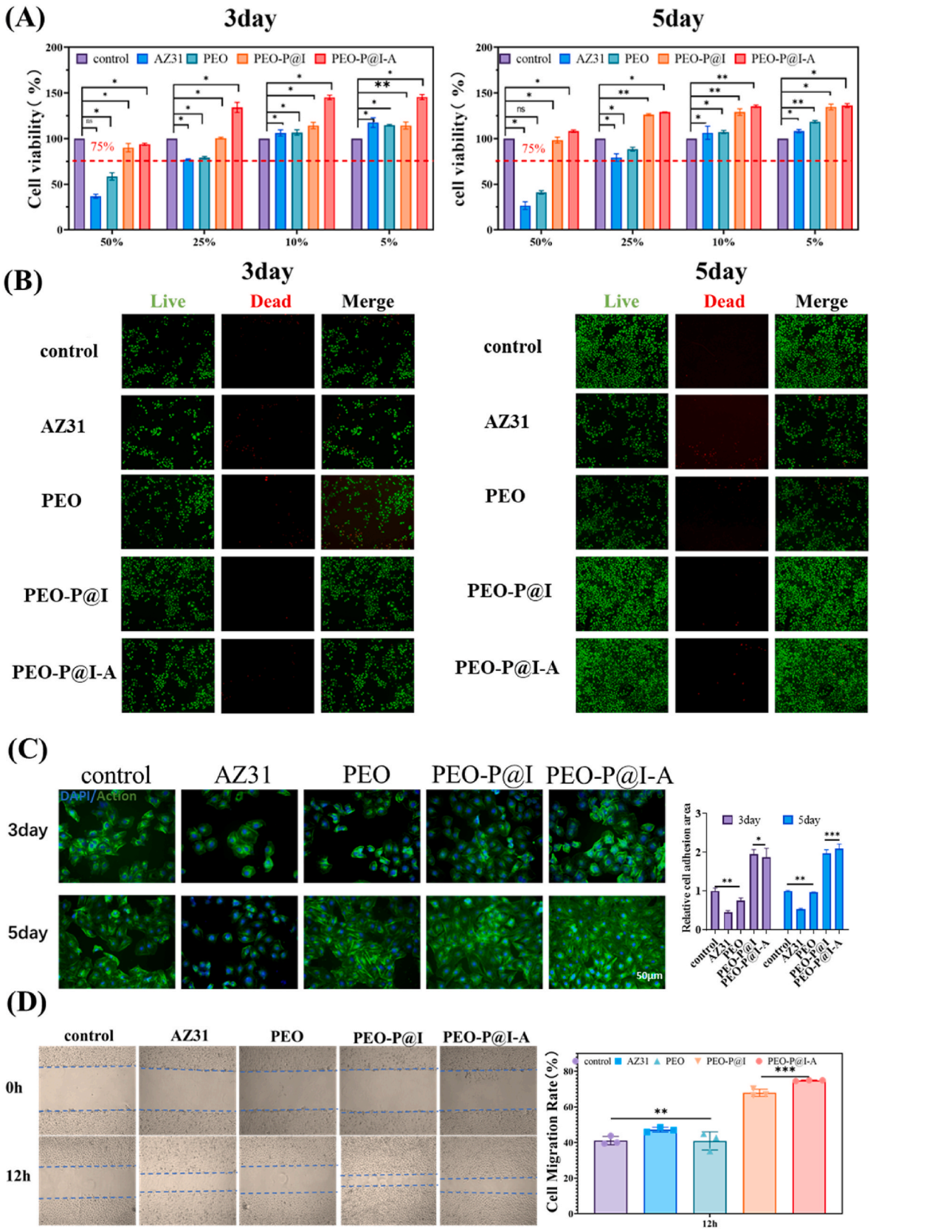


Fig. 13. In vitro cytocompatibility of AZ31, PEO, PEO-P@I and PEO-P@I-A extract culture with HUVECs. (A) Cell viability. (B)Live (green)/dead (red) staining of HUVECs after 3 and 5 days of incubation; (C)FITC (green)/DAPI (blue) staining of HUVECs after 3 and 5 days of incubation and quantitative data of cell adhesion number; (D) HUVECs Cell migration assays(0-12h).

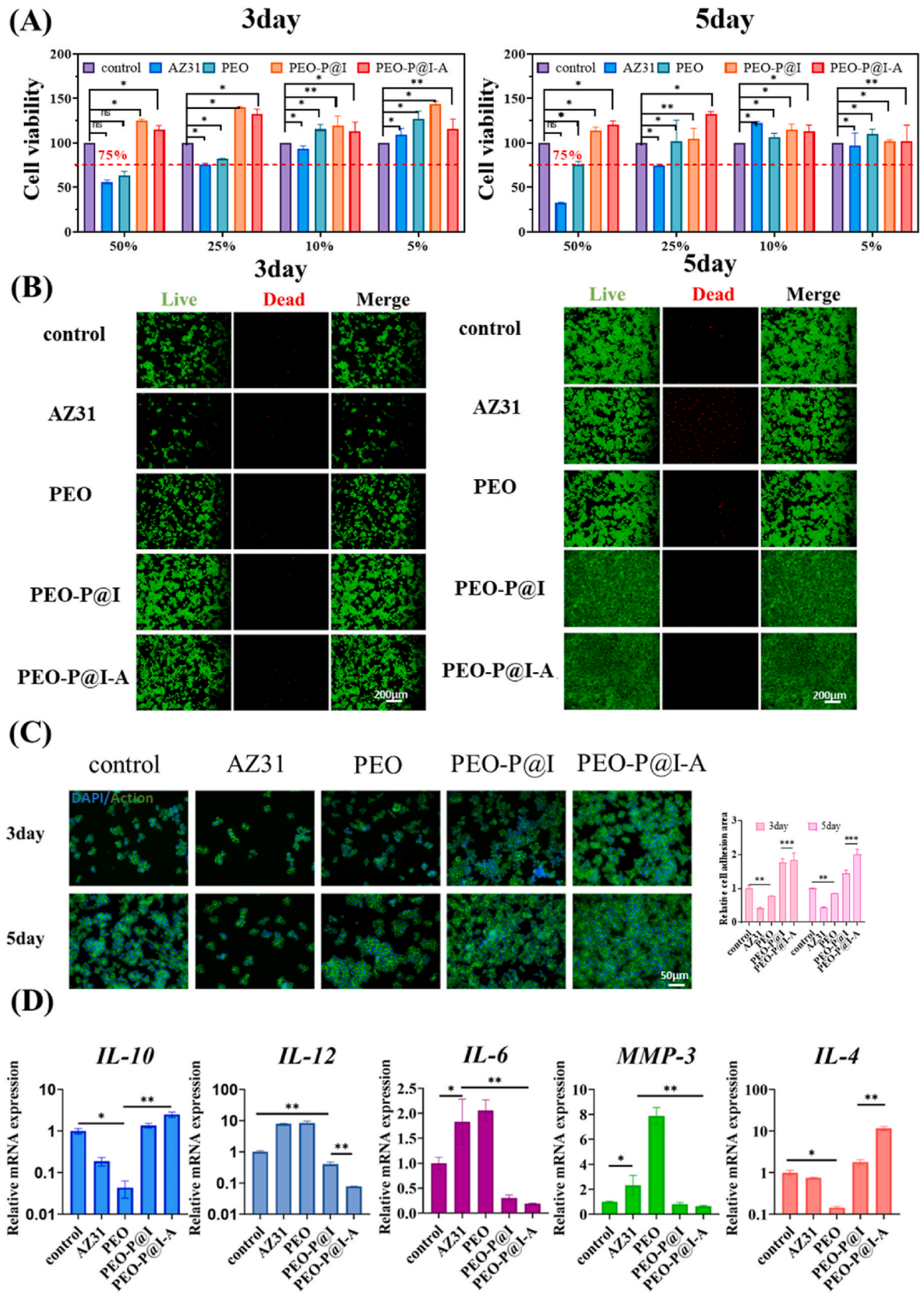


Fig. 14. In vitro cytocompatibility of AZ31, PEO, PEO-P@I and PEO-P@I-A extract culture with RAW264.7. (A) Cell viability after 3 and 5 days of incubation; (B) Live (green)/dead (red) staining of RAW264.7 after 3 and 5 days of incubation; (C)FITC (green)/DAPI (blue) staining of RAW264.7 after 3 and 5 days of incubation and quantitative data; (D)The qPCR results for the relative mRNA expression of angiogenesis-related genes, including IL-10, IL-12, IL-6, IL-4and MMP-3 after 7 days of incubation.

is even more pronounced, showing an 83.5% reduction ($p < 0.01$). Concurrently, MMP-3 expression is significantly reduced, by 5.1 ± 0.7-fold ($p < 0.05$), suggesting that the material may mitigate extracellular matrix degradation by inhibiting matrix metalloproteinase activity. Regarding anti-inflammatory cytokine regulation, the PEO-P@I-A group exhibits significant promotion: IL-4 and IL-10 expression levels increase 3.9 ± 0.6-fold and 7.8 ± 0.2-fold, respectively ($p < 0.01$). This differential regulatory pattern suggests potential mechanisms for the immunomodulatory action of the composite coatings: (1) Rapid suppression of IL-6 and IL-12 expression indicates possible inhibition of the inflammatory response via modulation of the NF-κB signalling pathway; (2) Sustained promotion of IL-10 expression implies potential involvement of STAT3 pathway activation. Significantly, the synergistic suppression of IL-6 and MMP-3 ($p < 0.01$) may collectively attenuate tissue damage within the inflammatory microenvironment, while the observed upregulation of IL-10 coupled with the downregulation of IL-12 ($p < 0.05$) reflects the material's ability to reprogram macrophage immune balance.

3.4.4. Antibacterial efficacy

The antibacterial efficacy of the composite coatings is evaluated through in-vitro experiments against *Staphylococcus aureus* (*S. aureus*) and *Escherichia coli* (*E. coli*), as depicted in Fig. 15. *E. coli* and *S. aureus* are co-cultured with different samples for 6, 12, and 24 h. The bacterial viability is subsequently assessed using the standard plate-colony counting technique to determine the antibacterial capacities of the samples (Fig. 15A and B).

The AZ31 group exhibits moderate antibacterial activity, achieving approximately 85% inhibition against both *S. aureus* and *E. coli.* This is presumably attributed to the corrosion of AZ31 upon contact with the bacterial suspension, leading to localized pH elevation and Mg-ion release, both factors known to inhibit bacterial growth. The inhibition rate for the PEO group drops to about 60%, due to the coating's ability to slow excessive corrosion of the Mg substrate and its lack of inherent antibacterial properties. In contrast, the PEO-P@I group exhibits significantly enhanced antibacterial efficacy, with inhibition rates exceeding 95%, attributable to the antibacterial activity of the ICA. Surface grafting of AMPs further boosts the antibacterial capability of the PEO-P@I-A sample, achieving an inhibition rate of approximately 99%. To further validate these findings, live/dead fluorescent staining is performed on *S. aureus* and *E. coli* after 24 h of culture (Fig. 15C). The PEO-P@I and PEO-P@I-A groups show significantly more yellow fluorescent spots than the AZ31 and PEO groups, confirming their superior antibacterial efficacy.

The antibacterial stability of the coatings is evaluated by immersing the samples in PBS for 3, 5, and 7 days. After immersion, the samples are co-cultured with *S. aureus* and *E. coli* for 24 h, followed by characterization using the plate-counting method (Fig. 15D and E). The antibacterial capability of AZ31 gradually diminishes during immersion, likely because the accumulating corrosion products cover the substrate surface, reducing its inhibitory effect on bacteria. The PEO group maintains inhibition rates between 50% and 62%. Both the PEO-P@I and PEO-P@I-A groups show a slight decrease in the antibacterial activity, potentially resulting from drug release during the immersion period. Nevertheless, both coatings retain high efficacy, demonstrating inhibition rates consistently above 85% after 7 days' immersion.

3.5. In-vivo performance

The in-vivo synergistic antibacterial and osteogenic properties of the PEO-P@I-A were evaluated using a 3 mm full-thickness critical-sized bone-defect model in SD rat femoral condyles, infected with *S. aureus* (Fig. 16A). Macroscopic observations of the implantation sites on post-operative days 3 and 7 (Fig. 16B) reveal distinct signs of acute infection in the group implanted with the PEO. These signs include pronounced erythema, subcutaneous pus accumulation, and exudation of yellowish-white purulent discharge. In contrast, the PEO-P@I-A group exhibits only mild erythema and minimal serous effusion, with no evidence of significant suppurative infection. Quantitative bacteriological analysis of the wound exudates collected on post-operative day 7 demonstrates a significantly lower number of colony-forming units in the PEO-P@I-A group, compared to both the untreated control and PEO groups ($p < 0.01$), robustly confirming the persistent antibacterial efficacy of the composite coating in-vivo.

Micro-CT imaging conducted 7 days post-implantation offers additional insights (Fig. 16C). Compared to the control and PEO groups, which display reduced bone density and osteolysis, the AZ31 group exhibits relatively milder bone resorption. This could be attributed to the antibacterial effect resulting from the high alkalinity or elevated Mg-ion concentration during degradation. Notably, the PEO-P@I-A group presents normal CT morphology, indicating that the early-stage release of antimicrobial agents from the coating successfully suppresses bacterial proliferation at the implant site.

X-ray radiographs taken 8 weeks post-implantation (Fig. 17A) reveals a low-density circular cavity surrounding the implanted AZ31, likely caused by hydrogen-gas accumulation because of rapid alloy degradation. The other groups, including PEO-P@I-A, do not display such distinct, persistent cavities, suggesting progressive filling by mineralized tissue and successful bridging of the defect between the implant and newly formed bone. Further analysis via Micro-CT at the 8 week time point (Fig. 17B) and subsequent statistical analyses of parameters including bone mineral density (BMD), bone volume/tissue volume (BV/TV), trabecular separation (Tb. Sp), and bone surface to bone volume ratio (BS/BV) provides three-dimensional structural evidence of new bone formation (Fig. 17B). The results suggest significant bone ingrowth into the defect area, with newly formed trabeculae connecting to the host bone. Specifically, the BMD of the regenerated bone around the PEO-P@I-A implants is higher than that in the AZ31 and control groups at 8 weeks. The BV/TV ratio follows the same trend. Furthermore, the analysis of Tb.Sp and BS/BV indicates that the PEO-P@I-A group is more conducive to the formation of peri-implant trabeculae, effectively promoting the regeneration of new bone tissue. These findings confirm the osteoconductive and osteoinductive properties of the PEO-P@I-A group.

Histological analyses employing hematoxylin and eosin (H&E) and Masson staining is conducted to evaluate bone-tissue regeneration around the implants at 8 weeks (Fig. 17C). H&E staining shows extensive new bone formation in the defect area of the PEO-P@I-A group, in contrast to minimal or absent bone formation in the AZ31 and control groups. Masson staining at 8 weeks indicates the deposition of blue-stained collagen fibres–a fundamental precursor and component of mature bone matrix—in the PEO-P@I-A group, confirming an active and high-quality osteogenic process. In contrast, the AZ31 and control groups exhibit no apparent collagen fibre proliferation at this early stage.

To assess potential systemic side effects of the composite coating, H&E staining is performed on cross-sections of the heart, liver, spleen, lung, kidney, and brain from all animal groups (Fig. 18A). No significant histopathological abnormalities, cell necrosis, or tissue damage are observed in any of the examined organs. These results clearly demonstrate that the implanted material does not induce systemic toxicity in the recipients. In summary, this surface-modified AZ31 alloy implant establishes a novel 'temporal' therapeutic strategy for treating infected bone defects. The drug-loaded coating based on PEO treatment successfully achieves three functions: it serves as an antibacterial barrier during the critical early phase, transitions into an osteogenic scaffold during the mid-to-late repair stages, and acts as a protective layer throughout the process to ensure controlled degradation and biocompatibility.

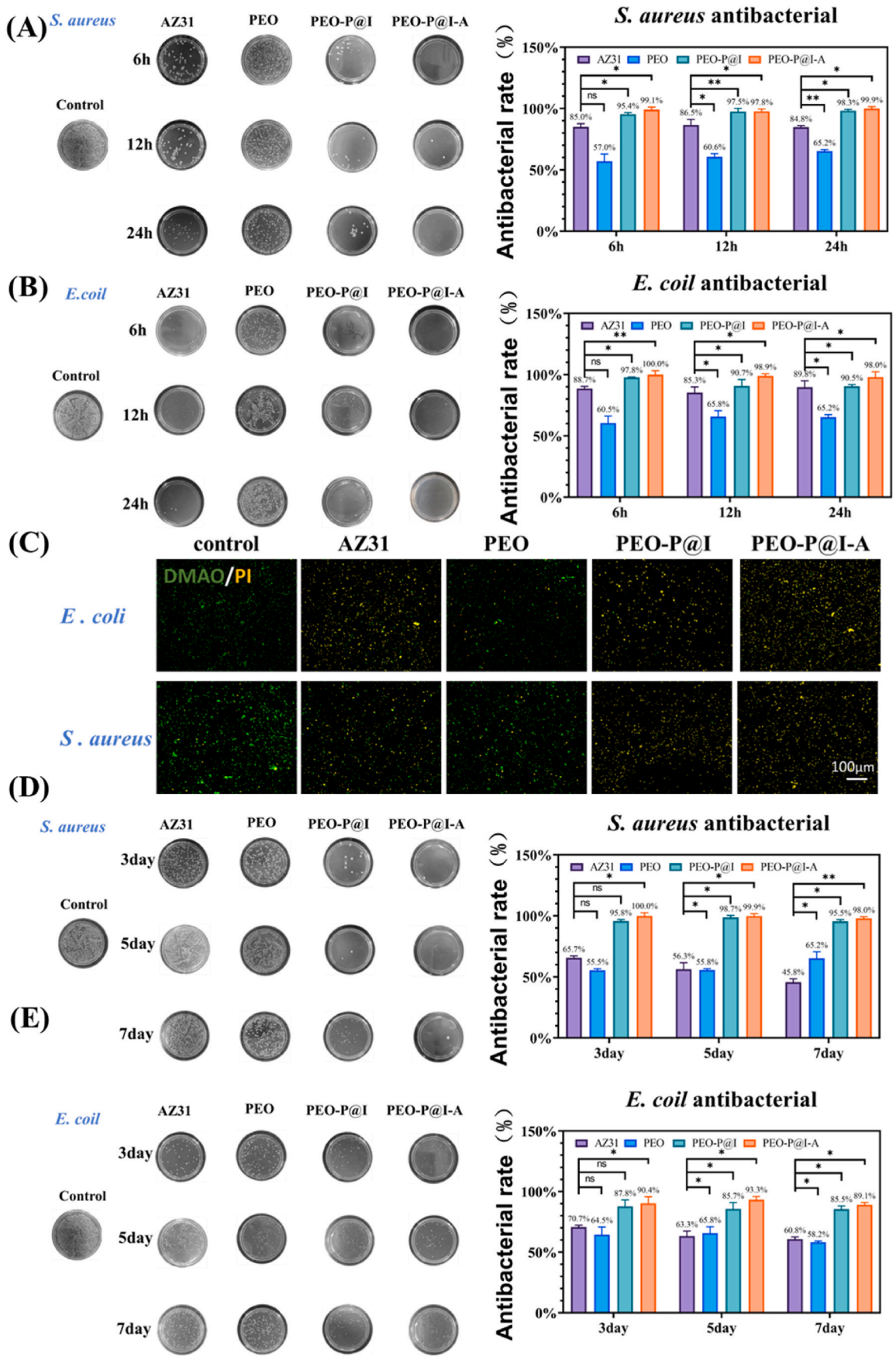


Fig. 15. (A) *E. coli* 6-24 h Plate count and antibacterial rate; (B) *S. aureus* 6-24 h Plate count and antibacterial rate; (C) 24 h Bacterial live-death staining; (D) *E. coli* 3-7day Plate count and antibacterial rate; (E) *S. aureus* 3-7day Plate count and antibacterial rate.

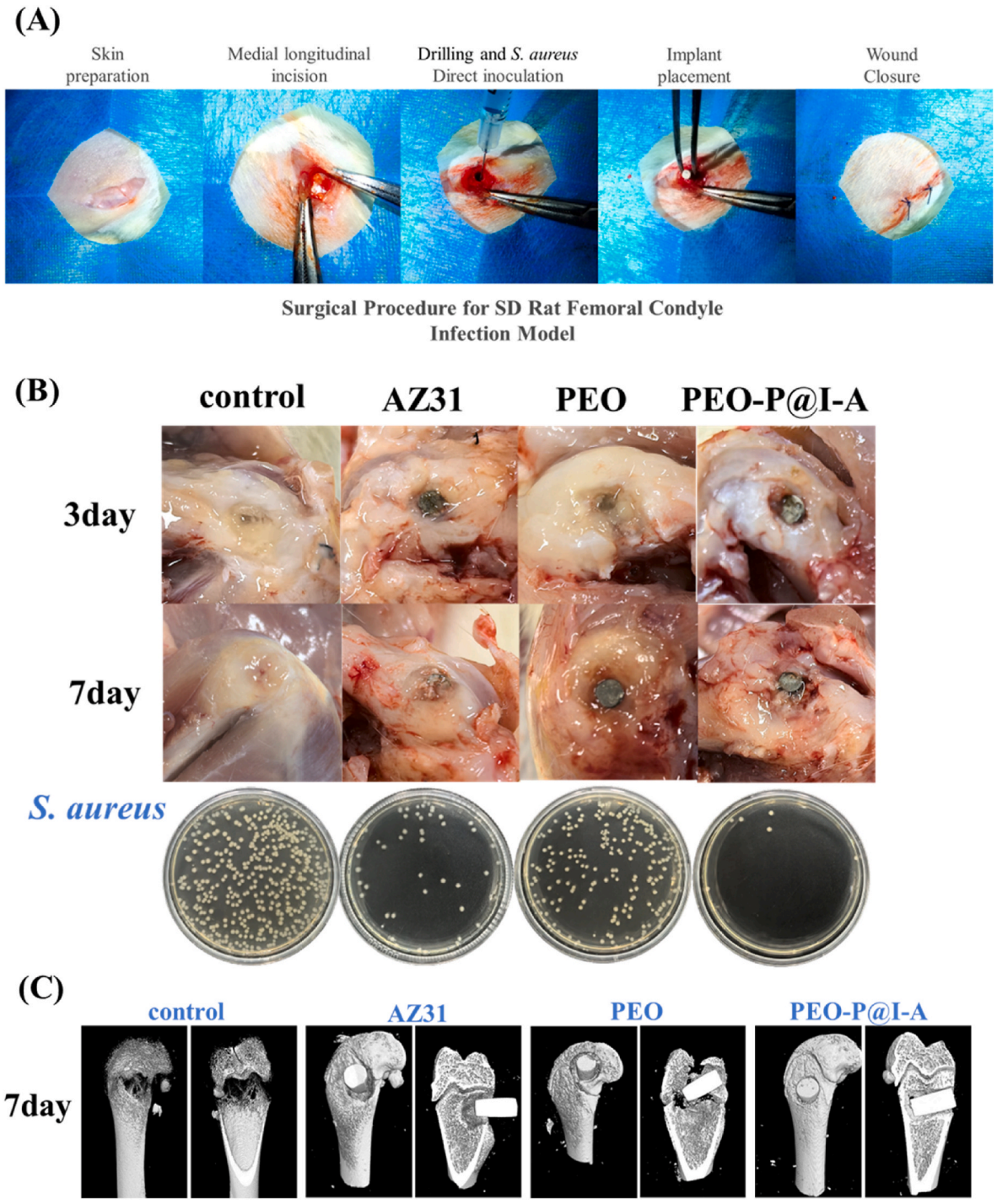


Fig. 16. (A) Modeling and implantation of infected femoral condyle defects; (B) Implantation site of infected femoral condyle (3-7 days); (C) Micro-CT of the infection site at 7 days post-implantation in the infected femoral condyle.

4. Discussion

4.1. Influence mechanism of coating design on corrosion resistance

The composite coating significantly enhanced the corrosion resistance of AZ31 alloy. The i_{corr} of bare AZ31 was 2.57×10^{-5} A/cm^2, while that of PEO-P@I and PEO-P@I-A coatings decreased to 1.96×10^{-9} and 1.54×10^{-9} A/cm^2 respectively, with a corrosion inhibition efficiency of 99.99% (Fig. 6A, Table 2). The low-frequency impedance modulus of the composite coatings (Fig. 6B–D) was approximately 3 orders of magnitude higher than that of AZ31, and remained above 10^6 Ω cm^2 during the 21-day immersion in SBF (Fig. 8), demonstrating excellent and stable barrier performance. The PTMC coating effectively protected the corrosion of the PEO in the dynamic degradation test. The PTMC-PEO composite mechanism exhibits a synergistic effect: the inner ceramic layer, with high hardness and excellent corrosion resistance, has a porous structure that provides a mechanical locking effect, better anchoring the intermediate layer; the outer polymer layer, with high flexibility and sealing properties, blocks corrosive media from entering through the PEO micropores, further enhancing the corrosion resistance of the coating.

The significant improvement in corrosion resistance is attributed to

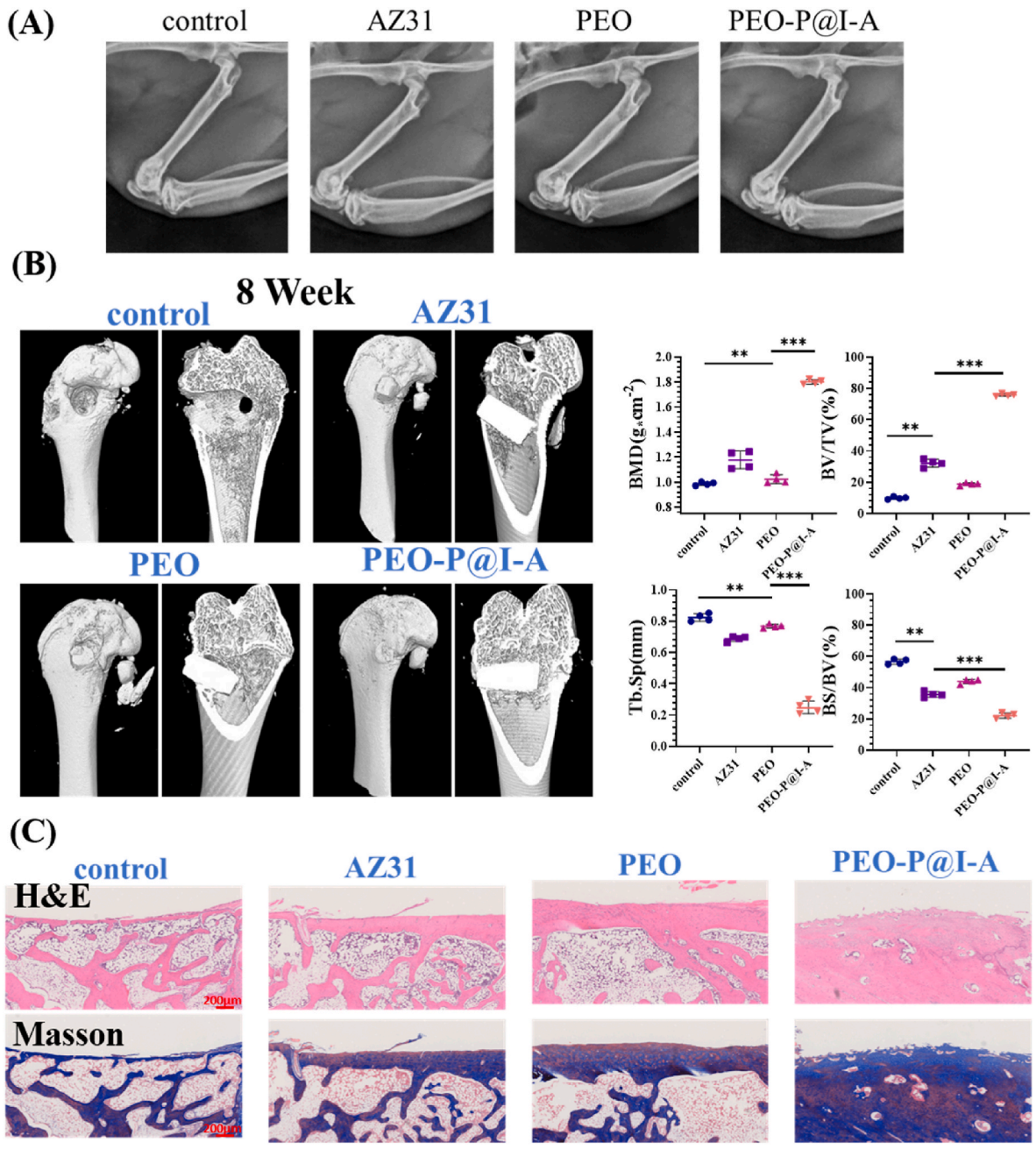


Fig. 17. In vitro cytocompatibility of AZ31, PEO, and PEO-P@I-A extract culture with RAW264.7. (A) X-ray of the infection site at 8 weeks post-implantation in the infected femoral condyle; (B) Micro-CT of the infection site at 8 weeks post-implantation in the infected femoral condyle; (C) H&E staining and Masson staining of the infection site at 8 weeks post-implantation in the infected femoral condyle.

the synergistic effect of the structure and components of the coating. (1) PEO layer: A ceramic layer mainly composed of MgO through micro-arc oxidation (Fig. 4B). Although its porous structure (Fig. 2) cannot completely block the corrosive medium [69], it provides a good mechanical interlocking substrate for the subsequent polymer coating, enhancing the adhesion between the film and the substrate [70] (Fig. 3). (2) PEO-P-I polymer coating: As a hydrophobic polymer, PTMC forms a dense, uniform coating (~45.8 μm in thickness, Fig. 3) on the PEO surface, significantly increasing the water contact angle from 40° to 70° (Fig. 4C). This polymer coating effectively seals the micropores and discharge channels of the PEO layer, acting as a robust barrier that greatly retards the ingress of corrosive species such as Cl^- and H_2O into the substrate [71,72]. "Moreover, the ICA structure contains multiple phenolic hydroxyl groups and carbonyl groups, which have the potential to chelate metal ions. This complexation mechanism—involving coordination of phenolic hydroxyl groups with Mg^{2+} ions—enables ICA to form stable metal-phenolic complexes at the substrate interface when Mg^{2+} is released through micro-defects, potentially creating a secondary protective barrier that further enhances corrosion resistance stability. The presence of aromatic C–OH (533.7 eV) and O═C–O (531.6 eV) functionalities in the O 1s XPS spectra (Fig. 5F and H) supports the presence of these chelating groups within the coating." During the long-term immersion, both the bare AZ31 and PEO showed significant pH increase, extensive hydrogen evolution, and surface corrosion product deposition (Fig. 7). However, the pH of the PEO-P@I and PEO-P@I-A remained stable at around 7.5 throughout 21 days, with a hydrogen evolution rate less than 0.012 ± 0.002 $mL*cm^{-2}*day^{-1}$, which is far below the threshold reported in literature [73] that causes

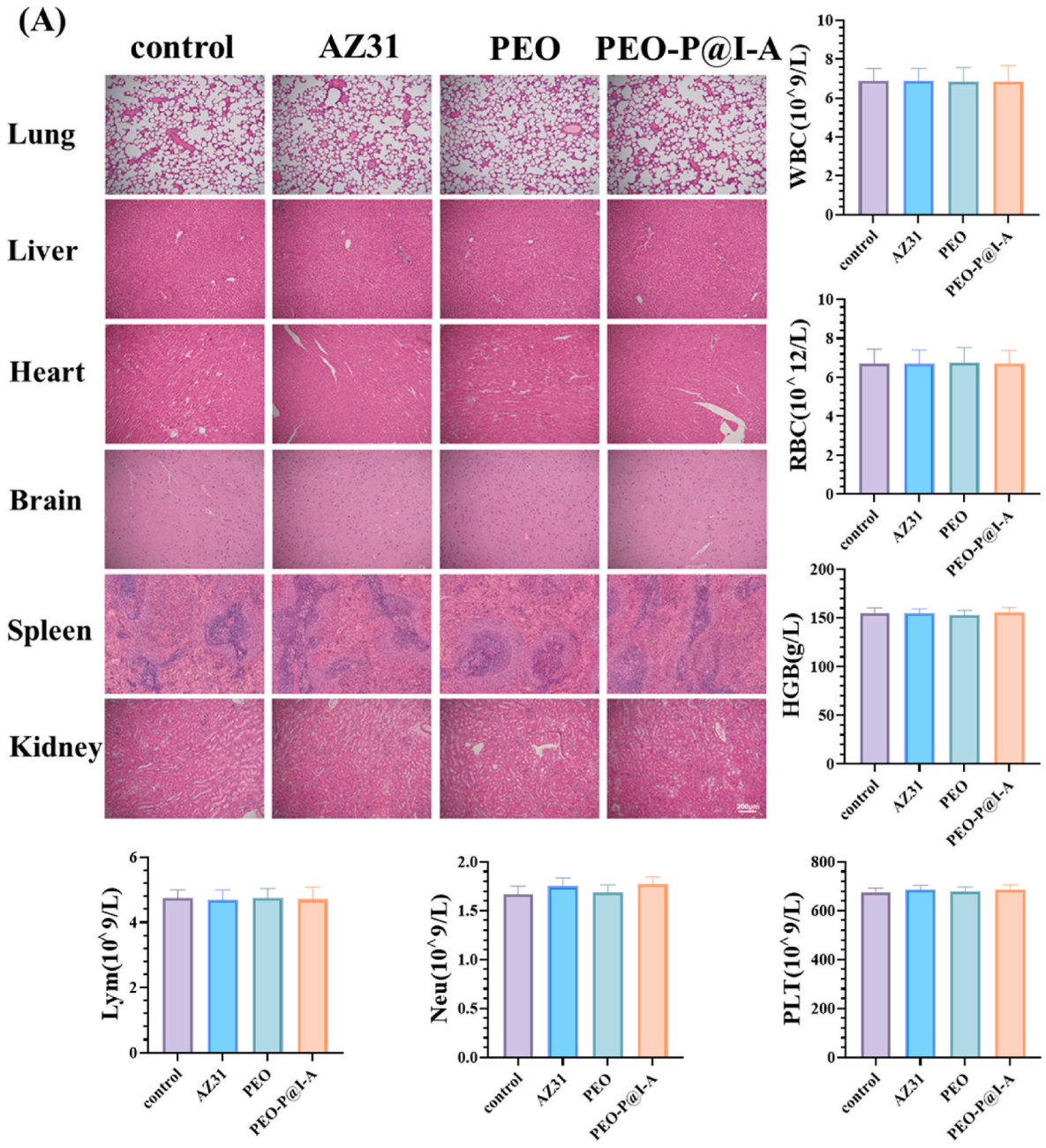


Fig. 18. (A) H&E staining of organs (heart, liver, spleen, lung, kidney, and brain) of SD rats at 8 weeks post-implantation.

inflammation in mice (0.068 mL*cm^{-2}*day^{-1}). (3) Effects of AMPs grafting: After AMPs were grafted, the hydrophilicity increased (the WCA decreased to 46.3°), attributed to the hydrophilic amino groups of AMPs [74], but it did not compromise its corrosion protection performance. On the contrary, the corrosion current density of PEO-P@I-A was slightly lower than that of PEO-P@I, and the hydrogen evolution amount (Fig. 9A) and the Mg^{2+} release concentration (Fig. 9D, cumulative release of approximately 36.1 mg/mL) during long-term immersion (21 days) were maintained at the lowest levels. This might be because the AMPs molecules further filled the microscopic defects on the PTMC surface, enhancing the barrier integrity. These results demonstrate that the "PEO-PTMC@ICA-AMPs" composite coating system effectively and sustainably controls the corrosion rate of the magnesium substrate through the dual effects of physical barrier and chemical stability, providing a prerequisite for maintaining the structural integrity and biological function of the implant in vivo [75–78].

Analogy with other PEO composite PTMC coating studies [79–81], The impedance value is increased by 3-4 orders of magnitude compared to AZ31 and by 1-2 orders of magnitude compared to PEO, and the PEO-P@I composite coating prepared in this study achieves the same level of corrosion resistance.

4.2. *Structure-dependent sequential functions of the coating*

Bone healing is a complex and dynamic biological process, involving stages such as inflammation, cartilage callus formation, hard callus formation, and bone remodeling, each with its unique biological functional requirements [82]. An ideal orthopedic implant should be able to meet the differentiated biological demands at healing stages: effectively prevent infection in the early postoperative period and actively promote bone integration in the middle and later stages. This study successfully endowed the material with this sequential function through a smart

"sandwich" coating component structure design [83–85].

In vitro antibacterial experiments demonstrated (Fig. 13) that the PEO-P@I-A coating had an inhibition rate of approximately 99% against *S. aureus* and *E. coli*, and maintained an antibacterial rate of over 85% after soaking in PBS for 7 days, indicating a sustained and stable antibacterial ability [86,87]. The results of the in vivo infection model further confirmed (Fig. 16) that the group implanted with the PEO-P@I-A coating only showed mild erythema in the early postoperative period, without signs of purulent infection, and the number of colonies in the wound exudate was significantly lower than that of the control group, proving its effective early antibacterial effect in a complex physiological environment.

It is worth noting that despite its strong antibacterial properties, the coating did not exhibit toxicity towards various mammalian cells. Cell compatibility experiments demonstrated (Figs. 11, 13 and 14) that at a 25% extract concentration, the survival rates of BMSCs, HUVECs, and RAW264.7 were all above 75% [88], and live-dead staining and phalloidin staining indicated that the cells were in a healthy state [89]. This suggests that the antibacterial effect of AMPs is selective [90], causing minimal damage to mammalian cell membranes. This selectivity arises from fundamental differences in membrane composition: bacterial membranes are rich in negatively charged phospholipids (e.g., phosphatidylglycerol and cardiolipin), while mammalian cell membranes predominantly contain zwitterionic phospholipids (e.g., phosphatidylcholine) and cholesterol. The cationic AMPs preferentially bind to the negatively charged bacterial membranes via electrostatic interactions, leading to membrane disruption, whereas the neutral or zwitterionic mammalian membranes are largely unaffected at the concentrations used.

As the coating gradually degrades, the loaded ICA and chemically grafted AMPs are released, thereby exerting their multi-functions: (1) Promoting osteogenic differentiation and mineralization: ICA significantly enhances the ALP activity of BMSCs (Fig. 11F) and the formation of mineralized nodules (ARS staining) [91], and upregulates the expression of key osteogenic genes (ALP, Runx2, OPN, Col-I) [92] (Fig. 11G). Notably, the expression of the Col-I gene is upregulated by 2.7 times, indicating that ICA can effectively promote collagen deposition and provide a scaffold for bone matrix formation [93]. The qPCR results show that the introduction of AMPs has a negligible effect on the osteogenic induction and mineralization promotion of ICA (only reducing by 2-5%), suggesting that the functional layering design of the coating is successful. (2) Inhibition of ferroptosis: ICA treatment notably reduced the Prussian blue-positive particles in BMSCs (Fig. 12A), upregulated the expression of anti-ferroptosis genes GPX4 and SLC7A11 [94], and concurrently downregulated the expression of pro-ferroptosis genes TFR1 and ACSL4 (Fig. 12B). These findings suggest that ICA protects osteoprogenitor cells against ferroptosis by modulating iron metabolism pathways, thereby establishing a more favorable microenvironment for bone regeneration. (3) Angiogenesis promotion: The extract of the composite coating significantly enhanced the viability, proliferation and migration ability of HUVECs (Fig. 13), indicating that ICA has the function of promoting endothelial cell activity [95], which is conducive to the formation of an early vascular network around the implant, providing nutrients and oxygen for bone tissue regeneration. (4) Immune regulation: The coating can guide macrophages to polarize towards an anti-inflammatory phenotype (Fig. 14D), the outer layer AMPs recognize and regulate macrophage activation pathways, guiding them to polarize towards the M2 anti-inflammatory phenotype, thereby significantly suppressing the expression of pro-inflammatory factors such as IL-6, IL-12, and MMP-3, while reducing excessive inflammation triggered by bacterial infection in the early stage of implantation; the intermediate layer releases ICA as an immunomodulatory flavonoid small molecule, further enhancing macrophage transformation to the anti-inflammatory phenotype, synergistically promoting the secretion of anti-inflammatory factors such as IL-4 and IL-10, improving the local immune microenvironment, and enhancing the osteogenic differentiation ability of mesenchymal stem cells. (5) In vitro antibacterial activity: The composite coating demonstrated rapid and long-lasting antibacterial capability in in vitro antibacterial evaluation. Within 24 h, the antibacterial rate against *Escherichia coli* and *Staphylococcus aureus* exceeded 98%, with AMPs exhibiting highly efficient and rapid antibacterial effects; meanwhile, the antibacterial rate remained above 90% over 7 days, showing that AMPs provide stable and long-lasting antibacterial effects. The outermost layer of AMPs creates an anti-infection implant microenvironment during the early implantation period.

The in vivo experimental results of the SD rat infectious bone defect model further verified the comprehensive biological functions of the coating. After 7 days of implantation (Fig. 16), compared with the positive control, AZ31, and the PEO group, the implantation site of the PEO-P@I-A coating showed no pus or white inflammatory exudate, a significant reduction in colony formation on plates, and, according to Micro-CT, no bone infection degradation was observed compared to the positive group, indicating that early AMP release effectively inhibits bacterial colonization and proliferation at the implantation site, preventing the occurrence of infectious bone destruction. After 8 weeks of implantation (Fig. 17), Micro-CT and histological analysis showed that the amount of new bone formed around the implant in the PEO-P@I-A group (BMD, BV/TV) was significantly higher than that in the control group, and the trabecular bone structure was denser and more continuous. At the same time, obvious collagen fiber deposition was observed (Masson staining), It indicates the continuous and stable release of ICA in the mid-to-late stage of implantation, accelerating collagen synthesis and mineralization, and significantly enhancing new bone formation and osseointegration. AMPs and ICA are sequentially released relying on the coating degradation process, further aligning with the healing process of bone defect repair, and the entire process of degradation is controllable, successfully constructing a sequential multifunctional composite coating on the implant surface. Compared with other sequential coating driving forces (bioactive factors, chemical catalysis, and physical excitation, etc. [96–102]), the use of coating degradation as the driving force offers distinct advantages for repairing infectious bone defects. This passive mechanism is intrinsically synchronized with the natural bone healing timeline: AMPs are released first during the early critical post-implantation period (1-7 days) when infection risk is highest, followed by sustained ICA release in the mid-to-late stages (2-8 weeks) when osteogenic, angiogenic, and immunomodulatory functions are most needed. This self-regulated temporal release requires no external intervention (unlike physical excitation) and avoids potential toxicity or complexity associated with chemical catalysts. By coupling drug release to the implant's natural degradation profile, our approach achieves a clinically relevant, patient-friendly sequential functionality that aligns seamlessly with the biological cascade of bone healing. We acknowledge that the exact in vivo timing of drug release and the mechanisms of their interaction warrant further detailed investigation. Nevertheless, our current experimental design provides a sufficient basis for claiming sequential functional switching: (1) in vitro ICA release data (Fig. 10) confirm sustained release over 14 days; (2) antibacterial stability tests (Fig. 15D and E) demonstrate that AMPs retain >85% activity after 7 days of pre-immersion; (3) in vivo results clearly show temporal separation of functions—infection prevention at day 7 (Fig. 16) and enhanced new bone formation at 8 weeks (Fig. 17); and (4) the coating's layered architecture inherently supports sequential release, with AMPs grafted on the outermost surface for immediate exposure and ICA embedded within the PTMC matrix for sustained release. Collectively, these results provide strong evidence for the intended sequential functionality, while future studies will precisely track in vivo drug release kinetics and the detailed molecular mechanisms of interaction.

5. Conclusion

In summary, this study successfully constructed a composite coating

on the surface of AZ31 alloy, which possesses both excellent corrosion resistance and sequential biological functions. The coating system operates through a synergistic multi-layer design: (1) the PEO layer serves as a corrosion-resistant ceramic base with a porous structure that provides mechanical interlocking for subsequent layers; (2) the intermediate PTMC + ICA layer acts as the primary corrosion barrier through its dense, hydrophobic nature, while also enabling sustained ICA release to promote osteogenesis, angiogenesis, and immune modulation in the mid-to-late stages; and (3) the outermost AMPs layer provides rapid, broad-spectrum antibacterial protection during the critical early post-implantation period. This dynamic functional transition—from early anti-infection to later osteogenesis promotion—is attributed to the controllable degradation characteristics of the coating, which are modulated by the sequential layering and the distinct degradation behavior of each component. Key quantitative results demonstrate the effectiveness of this design: the composite coating reduced the corrosion current density to 1.54×10^{-9} A/cm^2 (a 99.99% inhibition efficiency compared to bare AZ31) and maintained a low hydrogen evolution rate of 0.036 mL cm^{-2}·day^{-1} over 21 days. The AMPs conferred a near-complete antibacterial effect (~99% inhibition against *S. aureus* and *E. coli*) that remained above 85% even after 7 days of immersion. In vivo, the coating prevented infection and promoted significant new bone formation, achieving a bone volume fraction (BV/TV) of 22.7 ± 2.1% and a bone mineral density (BMD) of 0.38 ± 0.03 g/cm^3 at 8 weeks post-implantation, substantially higher than the infected control group. These quantitative metrics collectively validate the coating's potential for clinical translation in treating infected bone defects.

Declaration of competing interest

The authors declare that they have no known competing financial interests or personal relationships that could have appeared to influence the work reported in this paper.

Acknowledgments

Natural Foundation of Science and Technology Department of Sichuan Province (2026NSFSC0327), Vanadium–Titanium Materials Engineering Research Center of Sichuan province (25FTCLZX0015 and 25FTCLZX0016), Steel City Group Cooperation Project (HX2024132).

Appendix A. Supplementary data

Supplementary data to this article can be found online at https://doi.org/10.1016/j.jmrt.2026.07.118.

References

[1] Sarian MN, Iqbal N, Sotoudehbagha P, et al. Potential bioactive coating system for high-performance absorbable magnesium bone Implants. Bioact Mater 2022;12:42–63.
[2] Uppal G, Thakur A, Chauhan A, et al. Magnesium based implants for functional bone tissue regeneration – a review. J Magnesium Alloys 2022;10(2):356–86.
[3] Zhou K, Lu Q, Qin J, et al. A view of magnesium alloy modification and its application in orthopedic Implants. J Mater Res Technol 2025;36:1536–61.
[4] Antoniac I, Manescu (Paltanea) V, Antoniac A, et al. Magnesium-based alloys with adapted interfaces for bone implants and tissue engineering. Regen Biomater 2023;10.
[5] Chaudhari YS, Chaudhari MY, Gholap AD, et al. Surface engineering of nano magnesium alloys for orthopedic implants: a systematic review of strategies to mitigate corrosion and promote bone regeneration. Front Bioeng Biotechnol 2025;13.
[6] Tao M, Cui Y, Sun S, et al. Versatile application of Magnesium-related bone implants in the treatment of bone defects. Mater Today Bio 2025;31:101635.
[7] Dachasa K, Chuni Aklilu T, Gashaw Ewnete B, et al. Magnesium-based biodegradable alloy materials for bone healing application. Adv Mater Sci Eng 2024;2024(1).
[8] Saberi A, Baltatu MS, Vizureanu P. Recent advances in magnesium–magnesium oxide nanoparticle composites for biomedical applications. Bioengineering 2024;11(5):508.
[9] Yang C, Cui S, Fu RKY, et al. Optimization of the in vitro biodegradability, cytocompatibility, and wear resistance of the AZ31B alloy by micro-arc oxidation coatings doped with zinc phosphate. J Mater Sci Technol 2024;179:224–39.
[10] Lin Z, Zhao Y, Chu PK, et al. A functionalized TiO2/Mg2TiO4 nano-layer on biodegradable magnesium implant enables superior bone-implant integration and bacterial disinfection. Biomaterials 2019;219:119372.
[11] Liu C, Xu M, Wang Y, et al. Exploring the potential of Hydroxyapatite-based materials in biomedicine: a comprehensive review. Mater Sci Eng R Rep 2024;161:100870.
[12] Fu R, Zhao X, Liu Y, et al. An in silico model to examine the interaction between implant degradation and fracture healing under mechanical loading. Ann Biomed Eng 2025;53(8):1919–30.
[13] Taghipour S, Vakili-Tahami F, Allahverdizadeh A. Optimum design of a biodegradable implant for femoral shaft fracture fixation using finite element method. Phys Eng Sci Med 2025;48(3):999–1014.
[14] Wang Y, Li Z, Yu R, et al. Metal-phenolic network biointerface-mediated cell regulation for bone tissue regeneration. Mater Today Bio 2025;30:101400.
[15] Li Q, Wang X, Cao L, et al. Recent advances in the application of nanogenerators in orthopedics: from body surface to implantation. Nano Energy 2025;134:110542.
[16] Nilsson Hall G, Mendes LF, Gklava C, et al. Developmentally engineered callus organoid bioassemblies exhibit predictive in vivo long bone healing. Adv Sci 2019;7(2).
[17] Molitoris KH, Huang M, Baht GS. Osteoimmunology of fracture healing. Curr Osteoporos Rep 2024;22(3):330–9.
[18] Mao L, Hu Z, Song C. Biodegradable Mg-based medical devices: from passive support to active modulation. J Magnesium Alloys 2025;13(10):4795–816.
[19] Mohd Salaha ZF, Abdullah NNAA, Chan KF, et al. Biodegradable orthopaedic implants: a systematic review of in vitro and in vivo evaluations of magnesium, iron, and zinc alloys. Results Eng 2025;27:105746.
[20] Lu Y, Zhang T, Chen K, et al. Application of biodegradable implants in pediatric orthopedics: shifting from absorbable polymers to biodegradable metals. Bioact Mater 2025;50:189–214.
[21] Li P, Dai J, Li Y, et al. Zinc based biodegradable metals for bone repair and regeneration: bioactivity and molecular mechanisms. Mater Today Bio 2024;25:100932.
[22] Chen Q, Zou Z, Chen W, et al. Influence of PRP/GelMA-MAO composite coating on magnesium alloy implants in bone regeneration effect and bio-corrosion properties. J Mater Res Technol 2025;36:6874–89.
[23] Liu X, Ni G, Chen G, et al. Degradable magnesium implants with caerin 1.9-Polycaprolactone coatings provide extended antibacterial resistance and outstanding biocompatibility. Biomaterials Research; 2025. p. 29.
[24] Aikin M, Shalomeev V, Kukhar V, et al. Recent advances in biodegradable magnesium alloys for medical implants: Evolution, innovations, and clinical translation. Crystals 2025;15(8):671.
[25] Zheng Y, Liu X, Shen D, et al. Perceiving the connection between the bone healing process and biodegradation of biodegradable metal implants through precise bioadaptability principle. J Mater Sci Technol 2023;147:132–44.
[26] Chen H, Wang Y, He L, et al. Surface engineering of biodegradable magnesium alloys as orthopedic implant materials: recent developments and future prospects. Coatings 2025;15(2):191.
[27] Sampatirao H, Radhakrishnapillai S, Dondapati S, et al. Developments in plasma electrolytic oxidation (PEO) coatings for biodegradable magnesium alloys. Mater Today Proc 2021;46:1407–15.
[28] Piatkova MA, Nadaraia KV, Ponomarenko AI, et al. Hybrid surface layers with antibacterial and anti-inflammatory activity for implants materials. J Magnesium Alloys 2025;13(5):2343–57.
[29] Nadaraia MA, Mashtalyar DV, Golysheva AA, et al. Menaquinone-containing PDA-PEO coatings reduce corrosion of magnesium implants. Surf Interfaces 2026;85:108613.
[30] Tian P, Liu X, Ding C. In vitro degradation behavior and cytocompatibility of biodegradable AZ31 alloy with PEO/HT composite coating. Colloids Surf B Biointerfaces 2015;128:44–54.
[31] Monfared MM, Aghdam RM, Pishbin F, et al. Enhancement of PEO-coated ZK60 Mg alloy: curcumin-enriched mesoporous silica and PLA/bioglass for antibacterial properties, bioactivity and biocorrosion resistance. Surf Coating Technol 2024;493:131237.
[32] Wu G, Ibrahim JM, Chu PK. Surface design of biodegradable magnesium alloys — a review. Surf Coating Technol 2013;233:2–12.
[33] Keerthiga G, Prasad MJNV, Vijayshankar D, et al. Polymeric coatings for magnesium alloys for biodegradable implant application: a review. Materials 2023;16(13):4700.
[34] Streza A, Antoniac A, Manescu (Paltanea) V, et al. Effect of filler types on cellulose-acetate-based composite used as coatings for biodegradable magnesium implants for trauma. Materials 2023;16(2):554.
[35] Zhang Y, Zhang M, Li M, et al. Icariin-enhanced osteoclast-derived exosomes promote repair of infected bone defects by regulating osteoclast and osteoblast communication. Int J Nanomed 2024;19:12389–407.
[36] Luo Z, Chen X, Liu M, et al. The controlled release of a novel thiolated icariin for enhanced osteoporotic bone regeneration. Mater Des 2021;200:109468.
[37] Liu N, Huang S, Guo F, et al. Calcium phosphate cement with Icariin-loaded gelatin microspheres as a local drug delivery system for bone regeneration. Biomed Eng Online 2022;21(1).
[38] Xie D, Zhang Y, Lan X, et al. Identification of key ferrotoposis-related therapeutic targets in icariin efficacy for postmenopausal osteoporosis treatment. Pharmacol Res Mod Chin Med 2024;11:100427.

[39] Yao Z, Huang W, Yang Y, et al. Investigation of the osteogenic effects of ICA and ICSII on rat bone marrow mesenchymal stem cells. Sci Rep 2025;15(1).
[40] Wang F, Yang Z, Wei H, et al. Effects of icariin on the proliferation and osteogenic differentiation of human amniotic mesenchymal stem cells. Res Square Platform LLC 2020. 2020–10–13.
[41] Zhang J, Fan F, Liu A, et al. Icariin: a potential molecule for treatment of knee osteoarthritis. Front Pharmacol 2022;13.
[42] Chen Y, Pan X, Zhao J, et al. Icariin alleviates osteoarthritis through PI3K/Akt/mTOR/ULK1 signaling pathway. Eur J Med Res 2022;27(1).
[43] Wang H, Zhang H, Zhang Y, et al. Icariin promotes osteogenic differentiation of human bone marrow mesenchymal stem cells by regulating USP47/SIRT1/Wnt/B-catenin. Chem Biol Drug Des 2024;103(2).
[44] Xu Y, Jiang Y, Jia B, et al. Icariin stimulates osteogenesis and suppresses adipogenesis of human bone mesenchymal stem cells via miR-23a-mediated activation of the Wnt/β-catenin signaling pathway. Phytomedicine 2021;85:153485.
[45] Gao J, Xiang S, Wei X, et al. Icariin promotes the osteogenesis of bone marrow mesenchymal stem cells through regulating sclerostin and activating the Wnt/β-Catenin signaling pathway. BioMed Res Int 2021;2021(1).
[46] Xu L, Zeng Z. Role and application of Wnt/β-catenin signaling pathway in osteogenic differentiation of bone marrow mesenchymal stem cells [J]. Highlights in science. Eng Technol 2024;123:473–9.
[47] Yarahmadi HB, Khani A, Baghdadchi Y, et al. Study of the biological relevance of Wnt/β-catenin signaling pathway and β-adrenergic regulation in osteoblastic differentiation of mesenchymal stem cells. Gene Report 2022;29:101662.
[48] Bucataru C, Ciobanasu C. Antimicrobial peptides: opportunities and challenges in overcoming resistance. Microbiol Res 2024;286:127822.
[49] Yuan Z, Kang J, Wu S, et al. Advances in antimicrobial peptide-based biomaterials for combating multidrug-resistant bacterial infections. Macromol Rapid Commun 2025;46(14).
[50] Malekkhaiat Häffner S, Malmsten M. Influence of self-assembly on the performance of antimicrobial peptides. Curr Opin Colloid Interface Sci 2018;38:56–79.
[51] Chen R, Willcox MDP, Ho KKK, et al. Antimicrobial peptide melimine coating for titanium and its in vivo antibacterial activity in rodent subcutaneous infection models. Biomaterials 2016;85:142–51.
[52] Caselli L, Parra-Ortiz E, Micciulla S, et al. Boosting membrane interactions and antimicrobial effects of photocatalytic titanium dioxide nanoparticles by peptide coating. Small 2024;20(30).
[53] Ma X, Yang N, Mao R, et al. Self-assembly antimicrobial peptide for treatment of multidrug-resistant bacterial infection. J Nanobiotechnol 2024;22(1).
[54] Zhou W, Bai T, Wang L, et al. Biomimetic AgNPs@antimicrobial peptide/silk fibroin coating for infection-trigger antibacterial capability and enhanced Osseointegration. Bioact Mater 2023;20:64–80.
[55] Wu Y, She Y, Yan Z, et al. Facile construction of antimicrobial surface via one-step co-deposition of peptide polymer and dopamine. Macromol Biosci 2023;24(2).
[56] Yan C, Zhang J, An F, et al. Research progress of ferroptosis regulatory network and bone remodeling in osteoporosis. Front Public Health 2022;10.
[57] a Huang L, Wang J, Xu J, et al. Ferroptosis in osteogenic differentiation: A narrative review of bone regeneration Metabolism. Regen Med Rep 2025;2(3):100–7.b Wang Z, Yan Q, Wang Z, et al. Ferroptosis and its implications in Bone-related Diseases. PeerJ 2024;12:e18626.
[58] Xiao R, Han Z, Jia P, et al. Ferroptosis and bone health: bridging the gap between mechanisms and therapy. Front Immunol 2025;16.
[59] Tang Y, Su S, Yu R, et al. Unraveling ferroptosis in osteogenic lineages: implications for dysregulated bone remodeling during periodontitis progression. Cell Death Discov 2024;10(1).
[60] Huang J, Wu L, Zhao Y, et al. Programmed cell death of chondrocytes, synovial cells, osteoclasts, and subchondral bone cells in osteoarthritis. J Inflamm Res 2025;18:12323–60.
[61] Xiong Y, Chen L, Lin Z, et al. The regulatory role of ferroptosis in bone homeostasis. Stem Cell Int 2022;2022:1–9.
[62] Koehbach J, Craik DJ. The vast structural diversity of antimicrobial peptides. Trends Pharmacol Sci 2019;40(7):517–28.
[63] Luo Q, Yun Y, Fan W, et al. Application of near infrared spectroscopy for the rapid determination of epimedin A, B, C and icariin in epimedium. RSC Adv 2015;5(7):5046–52.
[64] Kuah KX, Wijesinghe S, Blackwood DJ. Toward understanding in vivo corrosion: influence of interfacial hydrogen gas build-up on degradation of magnesium alloy implants. J Biomed Mater Res 2022;111(1):60–70.
[65] Wang Z, Wang X, Pei J, et al. Degradation and osteogenic induction of a SrHPO4-coated Mg–Nd–Zn–Zr alloy intramedullary nail in a rat femoral shaft fracture model. Biomaterials 2020;247:119962.
[66] Ye J, Miao B, Xiong Y, et al. 3D printed porous magnesium metal scaffolds with bioactive coating for bone defect repair: enhancing angiogenesis and osteogenesis. J Nanobiotechnol 2025;23(1).
[67] He M, Chen L, Yin M, et al. Review on magnesium and Magnesium-based alloys as biomaterials for bone immobilization. J Mater Res Technol 2023;23:4396–419.
[68] Ayaz Z, Gong Y, Jiang Y, et al. Bioinspired surface modification of AZ31 Mg alloy with Cellulose-derivative HPMC: enhancing corrosion protection with biocompatibility. Surf Coating Technol 2025;496:131674.
[69] Iqbal MA, Matykina E, Arrabal R, et al. Role of anodic precursor layer thickness on PEO coatings: energy consumption and long-term corrosion performance. Surf Coating Technol 2024;476:130186.
[70] Croll SG. Surface roughness profile and its effect on coating adhesion and corrosion protection: a review. Prog Org Coating 2020;148:105847.
[71] Qian L, Sun M, Huang N, et al. Biodegradable PTMC-MAO composite coatings on AZ31 Mg-alloys for enhanced corrosion-resistance. J Alloys Compd 2024;998:175017.
[72] Ren J, Zhao Z, Li H, et al. Surface coatings on biomedical magnesium alloys. Materials 2025;18(14):3411.
[73] Witte F, Fischer J, Nellesen J, et al. In vitro and in vivo corrosion measurements of magnesium alloys. Biomaterials 2006;27(7):1013–8.
[74] Zhang W, Li J-X, Tang R-C, et al. Hydrophilic and antibacterial surface functionalization of polyamide fabric by coating with polylysine biomolecule. Prog Org Coating 2020;142:105571.
[75] Cao B, Cao L, Kallmes DF. Degradation rate assessment of biodegradable magnesium alloys. Mater Sci Appl 2024;15(8):245–52.
[76] Grewal NS, Sharma GK, Kumar K, et al. Thermally and mechanically tuned interfaces of magnesium alloys for bioimplant applications. Surf Interfaces 2023;41:103284.
[77] Das P, Kumar TSS, Sahu KK, et al. Corrosion, stress corrosion cracking and corrosion fatigue behavior of magnesium alloy bioimplants. Corrosion Rev 2022;40(4):289–333.
[78] Jana A, Das M, Balla VK. In vitro and in vivo degradation assessment and preventive measures of biodegradable Mg alloys for biomedical applications. J Biomed Mater Res 2021;110(2):462–87.
[79] Ye C, Wang J, Zhao A, et al. Atorvastatin eluting coating for magnesium-based stents: control of degradation and endothelialization in a microfluidic assay and in vivo. Adv Mater Technol 2020;5(3):1900947.
[80] Wang J, He Y, Maitz MF, et al. A surface-eroding poly(1,3-trimethylene carbonate) coating for fully biodegradable magnesium-based stent applications: toward better biofunction, biodegradation and biocompatibility. Acta Biomater 2013;9(7):8678–89.
[81] Feng M, Fu Q, Li J, et al. A micro-arc Oxidation/Poly(1,3-Trimethylene carbonate) hybrid coating for anticorrosion and hemocompatibility enhancement of high-purity magnesium. Metall Mater Trans 2024;55(4):1217–28.
[82] Garimella A, Bandhu Ghosh S, Bandyopadhyay-Ghosh S. Composite bone-implant engineered with magnesium and variable degradation for orthopaedics. Mater Today Proc 2023.
[83] Zhou W, Liu Y, Nie X, et al. Peptide-based inflammation-responsive implant coating sequentially regulates bone regeneration to enhance interfacial osseointegration. Nat Commun 2025;16(1).
[84] Chen B, Zhang L, Zhong Z, et al. Strontium/magnesium-doped coralline hydroxyapatite for bone regeneration. Regen Biomater 2025;12.
[85] Jin C, Liang J, Wu J, et al. Temporal immunomodulatory hydrogel regulating the immune-osteogenic Cascade for infected bone defects regeneration. Adv Mater 2025.
[86] Yang X, Niu X, Mo Z, et al. Electrochemical chiral interface based on the Michael addition/Schiff base reaction of polydopamine functionalized reduced graphene oxide. Electrochim Acta 2019;319:705–15.
[87] Erdem Büyükkiraz M, Kesmen Z. Antimicrobial peptides (AMPs): a promising class of antimicrobial compounds. J Appl Microbiol 2022;132(3):1573–96.
[88] Fan J, Schiemer T, Vaska A, et al. Cell via cell viability assay changes cellular metabolic characteristics by intervening with glycolysis and pentose phosphate pathway. Chem Res Toxicol 2024;37(2):208–11.
[89] Kalva SN, Uysal I, Khan SA, et al. Performance evaluation of 3D-printed PLA composites doped with WE43 magnesium alloy for bone tissue engineering applications. Biomater Adv 2025;177:214414.
[90] Bobone S, Stella L. Selectivity of antimicrobial peptides: a complex interplay of multiple equilibria [M]//Advances in experimental medicine and biology. Singapore: Springer; 2019. p. 175–214.
[91] Li H, Hu F, Liu Q, et al. Enhanced osteogenic differentiation for osteoporosis treatment through controlled icariin release in the bone cavity via extracorporeal shock wave. Nano Today 2024;58:102408.
[92] Xiao D, Huang S, Tang Z, et al. Mijiao formula regulates NAT10-mediated Runx2 mRNA ac4C modification to promote bone marrow mesenchymal stem cell osteogenic differentiation and improve osteoporosis in ovariectomized rats. J Ethnopharmacol 2024;330:118191.
[93] Zhao R, Bu W, Chen Y. Icariin treatment enhanced the skeletal response to exercise in estrogen-deficient rats. Int J Environ Res Publ Health 2019;16(19):3779.
[94] Xiao J, Luo C, Li A, et al. Icariin inhibits chondrocyte ferroptosis and alleviates osteoarthritis by enhancing the SLC7A11/GPX4 signaling. Int Immunopharmacol 2024;133:112010.
[95] Li N, Su S, Xie X, et al. Tsantan Sumtang, a traditional Tibetan medicine, protects pulmonary vascular endothelial function of hypoxia-induced pulmonary hypertension rats through AKT/eNOS signaling pathway. J Ethnopharmacol 2024;320:117436.
[96] Chen T, Jiang Y, Huang JP, et al. Essential elements for spatiotemporal delivery of growth factors within bio-scaffolds: a comprehensive strategy for enhanced tissue regeneration. J Contr Release 2024;368:97–114.
[97] Zeng Z, Hu C, Liang Q, et al. Coaxial-printed small-diameter polyelectrolyte-based tubes with an electrostatic self-assembly of heparin and YIGSR peptide for antithrombogenicity and endothelialization. Bioact Mater 2021.
[98] Prozzi M, Sordello F, Barletta S, et al. Assessing a photocatalytic activity index for TiO_2 colloids by controlled periodic illumination. ACS Catal 2020;10(16):9612–23.
[99] Razaviamri F, Singh S, Manuel J, et al. Utilizing rapid hydrogen peroxide generation from 6-Hydroxycatechol to design moisture-activated, self-disinfecting coating. ACS Appl Mater Interfaces 2024;16(21):26998–7010.

[100] Lee J, Kim D, Park M, et al. Spatiotemporally controllable electrical stimulator via independent photobending and upconversion photoluminescence using two different wavelengths of near-Infrared/Visible light as dual stimuli. ACS Appl Mater Interfaces 2023;15(39):46311–21.
[101] Liu P, Zhou T, Yang L, et al. Synergy of light and acid–base reaction in energy conversion based on cellulose nanofiber intercalated titanium carbide composite nanofluidics. Energy Environ Sci 2021;14(8):4400–9.
[102] Xie B, Hu D, Kumar P, et al. Heterogeneous catalysis via light-heat dual activation: a path to the breakthrough in C1 chemistry. Joule 2024;8(2):312–33.

Further reading

[1] Wang J, Xu J, Hopkins C, et al. Biodegradable magnesium-based implants in orthopedics—A general review and perspectives. Adv Sci 2020;7(8).
[2] Mousavian SMH, Bautin VA, Tabaian SH. Advanced strategies for Mg-based biodegradable implants: alloying, heat treatment, and coatings. J Alloys Compd 2025;1040:183575.
[3] Mhlongo JT, Waddad AY, Albericio F, et al. Antimicrobial peptide synergies for fighting infectious diseases. Adv Sci 2023;10(26).
[4] Caselli L, Traini T, Micciulla S, et al. Antimicrobial peptide coating of TiO_2 nanoparticles for boosted antimicrobial effects. Adv Funct Mater 2024;34(39).